Report

Cell Reports

PP2A-B55^{SUR-6} promotes nuclear envelope breakdown in *C. elegans* embryos

Graphical abstract

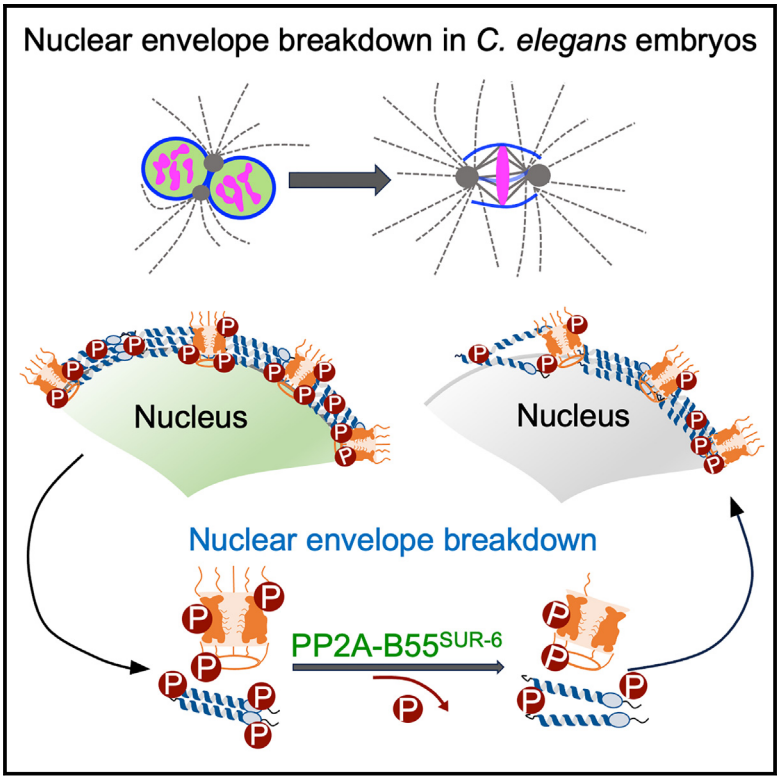

Authors

Sukriti Kapoor, Kuheli Adhikary, Sachin Kotak

Correspondence

sachinkotak@iisc.ac.in

In brief

Kapoor et al. demonstrate the essential role of phosphatase PP2A regulatory subunit B55^{SUR-6} in nuclear envelope breakdown (NEBD) in *C. elegans* embryos. They show that microtubule-dependent mechanical forces synergize with B55^{SUR-6} biochemical activity to promote NEBD, and nuclear lamin (LMN-1) is likely the target of B55^{SUR-6}.

Highlights

- PP2A regulatory subunit B55^{SUR-6} is essential for nuclear envelope breakdown (NEBD)
- B55^{SUR-6} promotes NEBD in a cell-cycle-independent manner
- B55^{SUR-6} synergizes with microtubule-based mechanical forces for efficient NEBD
- B55^{SUR-6} genetically and biochemically interacts with lamin

Kapoor et al., 2023, Cell Reports *42*, 113495
December 26, 2023
https://doi.org/10.1016/j.celrep.2023.113495

CellPress

Cell Reports

CellPress
OPEN ACCESS

Report

PP2A-B55^{SUR-6} promotes nuclear envelope breakdown in *C. elegans* embryos

Sukriti Kapoor,[1] Kuheli Adhikary,[1] and Sachin Kotak[1,2,*]
[1]Department of Microbiology and Cell Biology (MCB), Indian Institute of Science (IISc), Bangalore 560012, India
[2]Lead contact
*Correspondence: sachinkotak@iisc.ac.in
https://doi.org/10.1016/j.celrep.2023.113495

SUMMARY

Nuclear envelope (NE) disassembly during mitosis is critical to ensure faithful segregation of the genetic material. NE disassembly is a phosphorylation-dependent process wherein mitotic kinases hyper-phosphorylate lamina and nucleoporins to initiate nuclear envelope breakdown (NEBD). In this study, we uncover an unexpected role of the PP2A phosphatase B55^{SUR-6} in NEBD during the first embryonic division of *Caenorhabditis elegans* embryo. B55^{SUR-6} depletion delays NE permeabilization and stabilizes lamina and nucleoporins. As a result, the merging of parental genomes and chromosome segregation is impaired. NEBD defect upon B55^{SUR-6} depletion is not due to delayed mitotic onset or mislocalization of mitotic kinases. Importantly, we demonstrate that microtubule-dependent mechanical forces synergize with B55^{SUR-6} for efficient NEBD. Finally, our data suggest that the lamin LMN-1 is likely a bona fide target of PP2A-B55^{SUR-6}. These findings establish a model highlighting biochemical crosstalk between kinases, PP2A-B55^{SUR-6} phosphatase, and microtubule-generated mechanical forces in timely NE dissolution.

INTRODUCTION

Mitotic entry and its progression is a complex process, and a significant change in the phosphoproteome is required to orchestrate these events. Multiple kinases act together to bring about these changes and ensure that the duplicated genome is equally partitioned to the daughter cells post-mitosis. In metazoans, one pivotal event during mitosis is the nuclear envelope breakdown (NEBD), which allows microtubules to capture sister chromatids and assemble the mitotic spindle.[1–4] NEBD involves the systematic disassembly of the nuclear pore complexes (NPCs) and depolymerization of the lamina.[3,4] A tremendous effort in the past decades has linked several mitotic kinases, including cyclin-dependent kinase 1 (CDK-1), Polo-like kinase 1 (PLK-1), Aurora A kinase, and NIMA-related kinase (NEK) to NEBD.[5–16] These kinases promote hyperphosphorylation of the lamina and nucleoporins (NPPs), which are the subunits of NPC, resulting in the loss of nuclear integrity and intermixing of nuclear and cytosolic contents. In addition to kinases-dependent biochemical changes, microtubule and dynein-dependent mechanical forces are implicated in generating tension that facilitates NEBD.[17,18] However, whether kinases are the sole drivers of biochemical changes that help NEBD or this process also relies on additional modulators remains to be discovered. Also, if microtubule and dynein-dependent forces play a role in initiating NEBD beyond mammalian cells remains unknown.

Mitotic progression is equally dependent on the function of phosphatases. Dephosphorylation of substrates by the phosphatases is as tightly controlled as the phosphorylation reaction by the kinases, and thus, a critical balance between kinases and phosphatases action sets the level of phosphorylation on various substrates, which is essential for timely mitotic progression.[19–22] PP2A is one of the major phosphatases involved in mitosis.[23–29] PP2A is a trimeric complex consisting of a catalytic, a scaffold, and a variable regulatory subunit that provides substrate specificity.[19–21] Whether PP2A or phosphatases, in general, are involved in NE disassembly remains unknown.

Here, profiting from the highly stereotypical cell division of the one-cell *C. elegans* embryo, we discovered that B55^{SUR-6}, a regulatory subunit of PP2A, is essential for NEBD. In B55^{SUR-6}-depleted/mutated embryos, the lamina persists, and a subset of NPPs fails to disassemble, resulting in improper segregation of sister chromatids. The impact of B55^{SUR-6} on NEBD is not because of defective cell-cycle progression. Importantly, microtubules and dynein act synergistically with B55^{SUR-6} for efficient NE disassembly. Moreover, our genetic epistasis and biochemical experiments indicate that the lamin LMN-1 is likely a direct target of B55^{SUR-6}. In summary, our results indicate a vital function of an evolutionarily conserved PP2A regulatory subunit B55^{SUR-6} in NEBD and suggest a model wherein a biochemical tug-of-war between kinases and PP2A phosphatase together with microtubule-dependent mechanical forces ensures timely NEBD in animal cells.

RESULTS

PP2A regulatory subunit B55^{SUR-6} facilitates NE disassembly during mitosis

While studying the function of phosphatases during polarity establishment, we serendipitously noted that RNAi-mediated

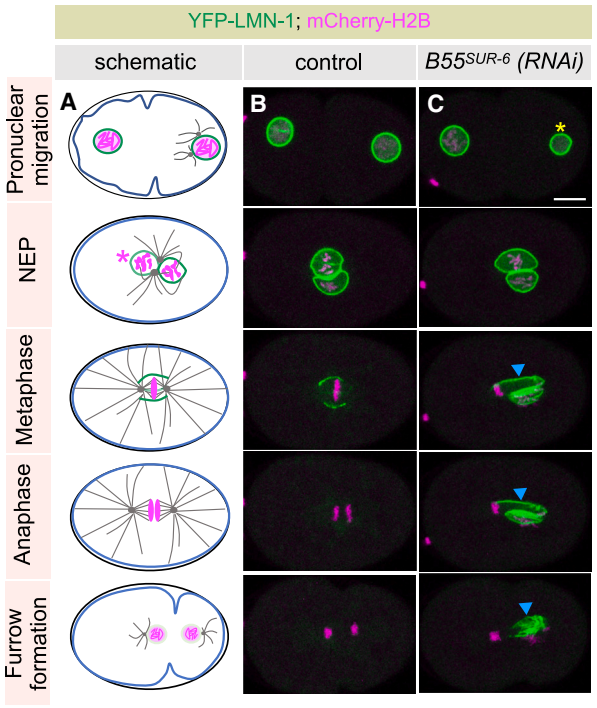

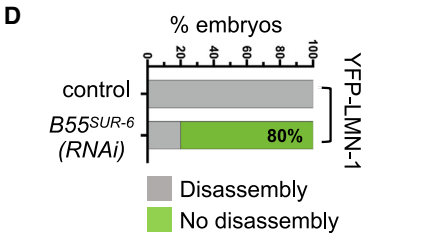

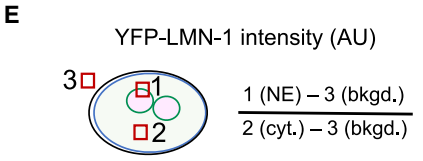

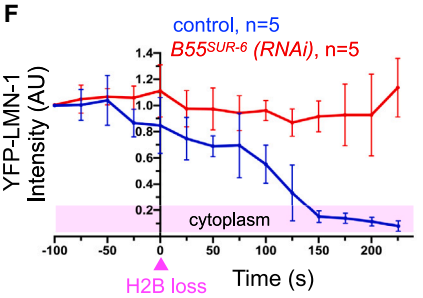

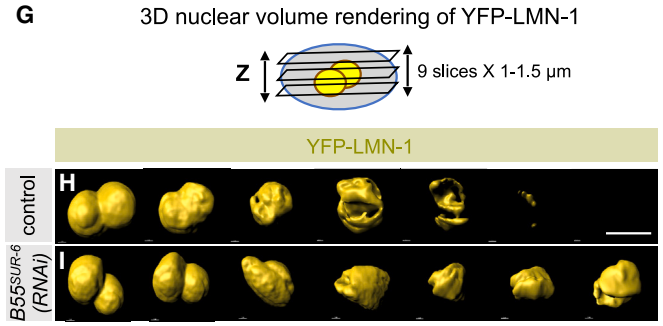

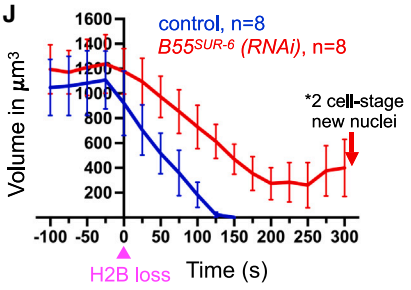

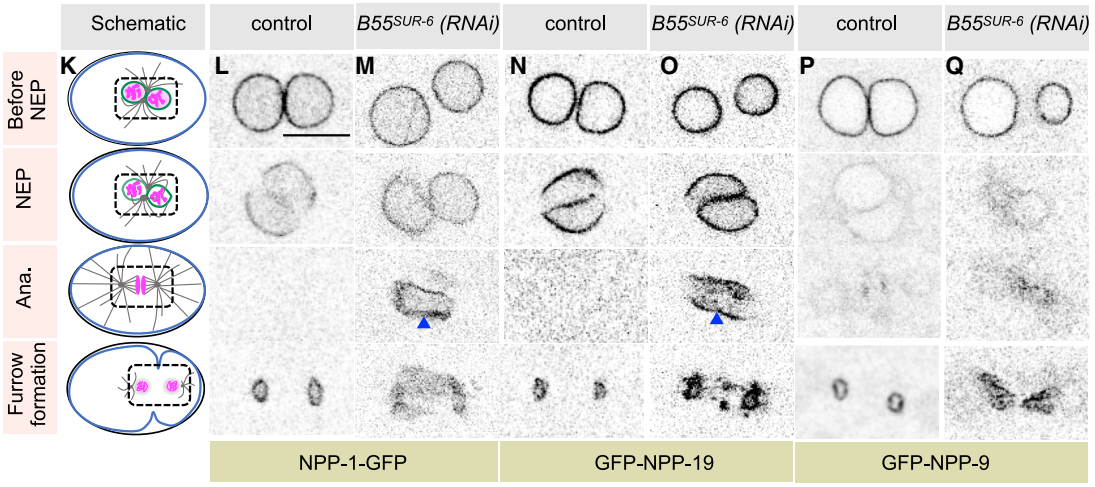

(legend on next page)

depletion of PP2A-regulatory subunit B55^{SUR-6} resulted in the appearance of multiple nuclei in the AB and P1 blastomeres at the two-cell stage (Figures S1A–S1C). This result is consistent with the previous observation in B55^{SUR-6} temperature-sensitive mutant or550 (referred to as *B55^{SUR-6}ts*) embryos (Figure S1C).[30] The occurrence of multiple nuclei in the AB/P1 blastomeres could be because of spindle assembly defects leading to chromosome segregation errors, or an inefficient NEBD, or a combination of both. To test these possibilities, we conducted the time-lapse recording in embryos expressing the microtubule marker GFP-tubulin or a kinetochore marker GFP-KNL-3, whose depletion has been associated with the kinetochore-null phenotype.[31,32] Although chromosomes fail to congress on the metaphase plate in embryos depleted for B55^{SUR-6}, we did not detect any significant change in microtubule nucleation capacity of the centrosomes or kinetochore localized KNL-3 levels upon B55^{SUR-6} depletion (Figures S1D–S1K). Similar observations were made for another kinetochore localized protein MEL-28, which is also an NPP (Figures S1L–S1N).[33] These data suggest that the occurrence of multiple nuclei in AB/P1 blastomeres upon B55^{SUR-6} depletion is unlikely due to defective microtubule nucleation capacity of centrosomes or abnormal kinetochore organization.

In *C. elegans* embryos, the permeability barrier of the nuclear envelope is breached at NEBD onset during prometaphase (referred to as NEP); however, the complete disassembly of the lamina occurs only ~200 s later during metaphase-to-anaphase transition.[7,8,34,35] To analyze the role of B55^{SUR-6} in NEBD, we utilized the *C. elegans* strain coexpressing the single B-type lamin YFP-LMN-1 and chromatin marker mCherry-H2B.[36,37] In control one-cell embryo, the female pronucleus is initially localized to the anterior after meiosis completion, and the male pronucleus is positioned at the posterior (Figures 1A and 1B). During prophase, the chromosomes condense while the two pronuclei migrate toward each other and meet at the embryo posterior. Together, the pronuclei then move to the embryo center and undergo NEBD, as monitored by the complete disappearance of the YFP-LMN-1 signal at the metaphase-to-anaphase transition (Figures 1A, 1B, and 1D; Video S1). Notably, the YFP-LMN-1 signal persists and never disappears during mitotic progression in a significant proportion (~80%) of B55^{SUR-6}-depleted embryos (Figures 1A, 1C, and 1D; Video S2). Quantification of the YFP-LMN-1 levels at the NE in control embryos revealed that the YFP-LMN-1 signal intensity progressively decreases ~50 s before nuclear envelope permeabilization (NEP) (Figures 1E and 1F). In contrast, YFP-LMN-1 intensity is maintained in embryos depleted for B55^{SUR-6} (Figures 1E and 1F). Next, to examine the impact of B55^{SUR-6} depletion on the 3D architecture of the two pronuclei, we performed volumetric analysis (Figure 1G). As expected, the nuclear hull volume persisted upon B55^{SUR-6} depletion despite the steady decrease over time (Figures 1H–1J).

B55^{SUR-6} inactivation leads to smaller size of male pronucleus (Figure 1C).[30,38] Thus, the persistent LMN-1 signal in B55^{SUR-6}-depleted embryos could be linked to defective male pronucleus. Therefore, we focused our attention on the female pronucleus and analyzed its growth after meiotic exit and its disassembly during mitotic progression in control and upon B55^{SUR-6} depletion (Figure S1O). The initial diameter and the growth kinetics of the female pronucleus in B55^{SUR-6}-depleted embryos were comparable to control embryos (Figure S1P). Importantly, we found that the B55^{SUR-6} function in LMN-1 disassembly is not restricted to the male pronucleus but equally impacts the female pronucleus (Figure 1C; Video S2). These results indicate that the role of B55^{SUR-6} in regulating male pronucleus size is distinct from its function in promoting NEBD.

We further sought to examine the role of B55^{SUR-6} in disassembling nucleoporins (NPPs) and inner nuclear envelope protein, Emerin during NEBD. To this end, we utilized strains expressing tagged nucleoporin of the central channel (NPP-1-GFP), the inner ring (GFP-NPP-19), or the cytoplasmic filaments (GFP-NPP-9) (Figure S1Q).[1] Analogous to LMN-1, the NE signal of NPP-1-GFP and GFP-NPP-19 persisted in the majority of B55^{SUR-6}-depleted embryos, in contrast to the control embryos (Figures 1K–1O). Likewise, the NPP-1-GFP signal was retained in 100% of *B55^{SUR-6}ts* mutant embryos (Figure S6B). Interestingly, the cytoplasmic nucleoporin GFP-NPP-9 signal disappeared in most of the B55^{SUR-6}-depleted embryos (Figures 1P and 1Q). Consistent with our analysis of NPP-1-GFP and GFP-NPP-19, we detected the abnormal persistence of multiple

Figure 1. B55^{SUR-6} is critical for the lamina and nucleoporins disassembly

(A–C) Schematics of cell-cycle stages (A) and the corresponding images from the time-lapse confocal microscopy of *C. elegans* embryos coexpressing YFP-LMN-1 (green) and mCherry-H2B (magenta) in control (B) and *B55^{SUR-6} (RNAi)* (C). The magenta asterisk in the schematic indicates NEP as monitored by the expulsion of the nucleoplasmic mCherry-H2B signal. The yellow asterisk indicates the smaller size of the male pronucleus in *B55^{SUR-6} (RNAi)*, and the blue arrowhead marks the persistence of LMN-1 signal. The scale bar in this and following panels represents 10 μm.

(D) Percentage [%] of control and *B55^{SUR-6} (RNAi)* embryos that fail NE disassembly (defined by persistence of YFP-LMN-1 NE signal) during metaphase-to-anaphase transition [n = 10 for control, n = 31 for *B55^{SUR-6} (RNAi)*].

(E and F) Schematics of the method used for quantifying YFP-LMN-1 fluorescence intensity on the NE (E), and the outcome of this analysis (F) in control (blue) and *B55^{SUR-6} (RNAi)* (red) embryos (bkgd.: background intensity; cyt.: cytoplasmic intensity). In this and (J), time "0" is NEP. Error bars, SD.

(G) Schematics of image acquisition parameter used to measure the nuclear hull volume (see STAR Methods).

(H and I) Three-dimensional rendered sections of the male and female nuclei just before NEP from (B) and (C) depicting YFP-LMN-1 NE signal in control (H) and in *B55^{SUR-6}* 1×10^{-6} *(RNAi)* embryos (I).

(J) Quantification of the nuclear volume (in μm^3) for control and *B55^{SUR-6} (RNAi)* embryos as indicated in (G). Error bars, SD.

(K–Q) Schematics of cell-cycle stages (K). The boxed sections in the schematics correspond to the images obtained from time-lapse confocal microscopy of embryos expressing NPP-1-GFP (L and M), GFP-NPP-19 (N and O), and GFP-NPP-9 (P and Q) in control and *B55^{SUR-6} (RNAi)* condition, as indicated. n = 20, control; n = 28, *B55^{SUR-6} (RNAi)* for NPP-1-GFP-expressing embryos (27/28 = 96.43% proportion of RNAi embryos retain NPP-1-GFP signal upon B55^{SUR-6} depletion). n = 7, control; n = 8, *B55^{SUR-6} (RNAi)* for GFP-NPP-19-expressing embryos (7/8; 87.5% proportion of RNAi embryos retain GFP-NPP-19 signal upon B55^{SUR-6} depletion). n = 9, control; n = 13, *B55^{SUR-6} (RNAi)* for GFP-NPP-9-expressing embryos (12/13; 93% of the B55^{SUR-6}-depleted embryos lose GFP-NPP-9 signal at the NE).

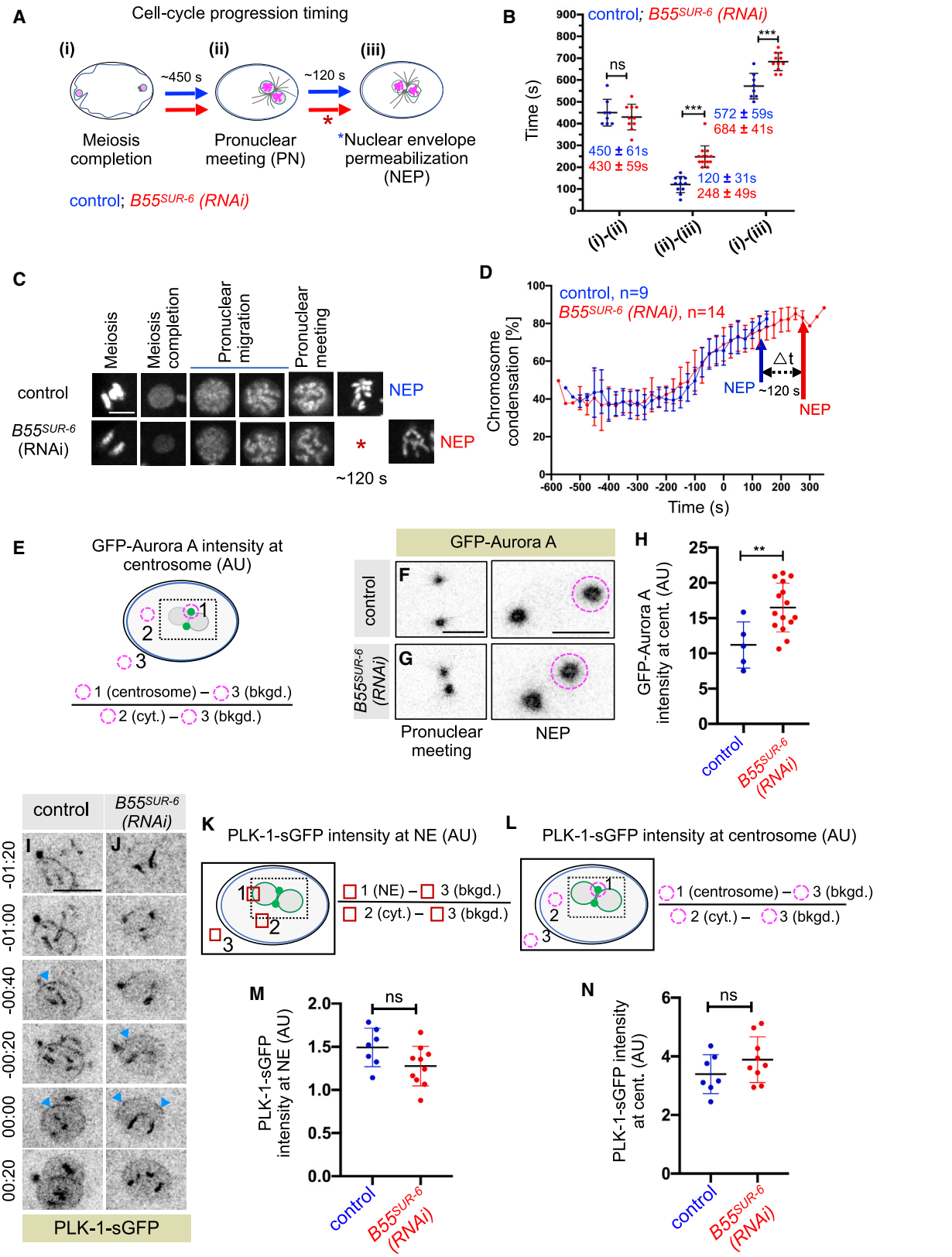

(legend on next page)

endogenous NPPs during anaphase in *B55^{SUR-6}ts* mutant using mAb414 antibodies (data not shown).[39,40]

Next, we analyzed the role of B55^{SUR-6} in Emerin disassembly. Similar to the previous observations, we noted that the nuclear membrane undergoes scission between the two pronuclei, allowing the mingling of both parental genomes in control embryos (Figures S1R and S1S).[11,15] However, this scission event failed to occur in a significant number of embryos depleted for B55^{SUR-6} (Figure S1T). Based on these results, we conclude that B55^{SUR-6} is essential for disassembling lamina, a subset of nucleoporins, and the inner nuclear envelope (NE) during mitotic progression.

B55^{SUR-6} role in NEBD is not via regulating mitotic entry

How does B55^{SUR-6} promote NEBD? Since CDK-1 activity is required for mitotic entry, chromosome condensation, and NEBD,[41,42] one possibility is that B55^{SUR-6} is required for CDK-1 activation and, therefore, indirectly regulates NEBD. To test this, we measured the interval between meiosis completion and pronuclear meeting in control and B55^{SUR-6}-depleted embryos as a proxy for CDK-1 activation.[7] The timing of meiosis completion to the pronuclear meeting in B55^{SUR-6}-depleted embryos was similar to control (Figures 2A and 2B). To test this rigorously, we used a well-established image analysis pipeline to quantify chromosome condensation in control and *B55^{SUR-6} (RNAi)* condition (Figure S2A, and STAR Methods).[7,43] The chromosome condensation kinetics of the female pronucleus in B55^{SUR-6}-depleted embryos were identical to that of control embryos (Figures 2C and 2D). Though we did not observe any abnormality related to chromosome condensation or the growth of the female pronucleus upon B55^{SUR-6} depletion, there was a specific and significant delay of ~120 s from the pronuclear meeting to NEP (Figures 2A, 2B, and S1P), suggesting that B55^{SUR-6} regulates the timing of NEBD onset.

Earlier work has demonstrated that NEP occurs in two phases. In the first phase, the outermost components of NPCs are released, which allows the entry of molecules less than 40 nm in diameter into the nucleus. This is followed by the complete removal of NPCs, which allows the entry of particles larger than 40 nm.[7,44,45] To determine B55^{SUR-6} role in NEP kinetics, we examined the nuclear accumulation of tetramethylrhodamine (TMR)-70 kDa dextran (hydrodynamic radius ~36 nm) and GFP-NMY-2 (hydrodynamic radius >40 nm), as a marker for the first and the second phase of nuclear permeabilization, respectively.[7,45,46] In control embryos, the time interval between TMR-dextran and GFP-NMY-2 nuclear entry is ~45 s, which remained unchanged upon B55^{SUR-6} depletion (Figures S2B–S2D), indicating that B55^{SUR-6} does not regulate the kinetics of NEP. Overall, these results indicate that the impact of B55^{SUR-6} depletion on NEP and lamina/nucleoporins/inner nuclear membrane disassembly is not due to delayed mitotic entry.

Aurora A and PLK-1 activity remain unchanged in B55^{SUR-6}-depleted embryos

Centrosome-localized active Aurora A is implicated in NEBD.[7,8] Therefore, we decided to explore if B55^{SUR-6} could act upstream of Aurora A to promote NEBD. Aurora A depletion leads to an ~7 min delay in NEP.[7,8] If B55^{SUR-6} would function upstream of Aurora A in controlling NEBD, we expect a reduction in centrosomal Aurora levels in B55^{SUR-6}-depleted embryos. However, we failed to see any decrease in GFP-Aurora A levels (Figures 2E–2H). In contrast, we noticed a slight, but significant increase in centrosomal GFP-Aurora A levels (Figure 2H). Interestingly, the slightly enriched Aurora A pools at the centrosomes in *B55^{SUR-6} (RNAi)* condition likely does not reflect increased Aurora A activity, as the levels of Aurora A substrates, TBG-1 and ZYG-9, remain unaltered (Figures S2E–S2K).[32,47] Moreover, the microtubule nucleation capacity of the centrosomes, which

Figure 2. B55^{SUR-6} depletion delays NEP without affecting the mitotic onset

(A) Schematic of the cell-cycle progression stages: meiosis completion (i), pronuclear meeting (ii), and NEP (iii).

(B) Quantification of the time interval between cell-cycle stages (i), (ii), and (iii) in control (blue circle) and *B55^{SUR-6} (RNAi)* (red circle) embryos. The time interval between stages (i) and (ii) in control (n = 8) and *B55^{SUR-6} (RNAi)* (n = 10) embryos is non-significant (ns). However, there is a significant increase in a time interval between stages (ii) and (iii) of ~120 s in *B55^{SUR-6} (RNAi)* (n = 14), compared with control embryos (n = 11). Consequently, this delay persists from stage (i) to (iii) in *B55^{SUR-6} (RNAi)* embryos (n = 11), compared with control embryos (n = 8). ns, $p > 0.05$; **, $p < 0.01$; ***, $p < 0.001$ as determined by two-tailed unpaired Student's t test.

(C) Nuclear insets of maximum z-projections from time-lapse confocal microscopy of control and *B55^{SUR-6} (RNAi)* embryos expressing GFP-H2B at various cell-cycle stages, as indicated. Asterisk indicates delayed NEP (~120 s) upon B55^{SUR-6} depletion compared with the control. Scale bar, 5 μm.

(D) Quantification of chromosome condensation [%] of the female pronucleus in control (blue, n = 9) and *B55^{SUR-6} (RNAi)* (red, n = 14) embryos over time. t = 0 on the x axis is pronuclear meeting, that remain unchanged in *B55^{SUR-6} (RNAi)*. Also, see Figure S2A, and STAR Methods. Error bars, SD.

(E) Schematic of the quantification method used to evaluate the GFP-Aurora A intensity at the centrosome in control and *B55^{SUR-6} (RNAi)* embryos (bkgd.: background intensity; cyt.:cytoplasmic intensity) at NEP.

(F–H) Images from time-lapse confocal microscopy of embryos expressing GFP-Aurora A in control (F) and *B55^{SUR-6} (RNAi)* (G) embryos. The dotted circle represents the area used for quantifying the GFP-Aurora A intensity. Quantification of GFP-Aurora A intensity at the centrosome (cent.) (H) in control (blue circle, n = 5) and *B55^{SUR-6} (RNAi)* (red circle, n = 15) embryos at NEP, monitored by the breakdown of the distinct contour of the nucleus in the Differential Interference Contrast (DIC) images (not shown). Scale bar, 10 μm. Error bars, SD; **p = 0.0075 as determined by two-tailed unpaired Student's t test.

(I and J) Images from the time-lapse confocal microscopy of embryos expressing PLK-1-sGFP in control (I) and *B55^{SUR-6} (RNAi)* (J) embryos. The blue arrowheads depict the NE. Time stamps are relative to NEP (00.00 s), which was monitored by the breakdown of the distinct contour of the nucleus in the DIC images (not shown). Scale bar, 10 μm.

(K–N) Schematic of the method used to quantify PLK-1-sGFP fluorescence intensity at the NE (K) and on the centrosomes (L). Quantification of PLK-1-sGFP intensity at the NE (M) and the centrosome (cent.) (N) in control (blue circle) and *B55^{SUR-6} (RNAi)* (red circle). n = 7 for control, and $n \geq 9$ for *B55^{SUR-6} (RNAi)* embryos (bkgd.: background intensity; cyt.: cytoplasmic intensity). Error bars, SD; p = 0.070 (at NE) and p = 0.202 (at centrosome), as determined by two-tailed unpaired Student's t test.

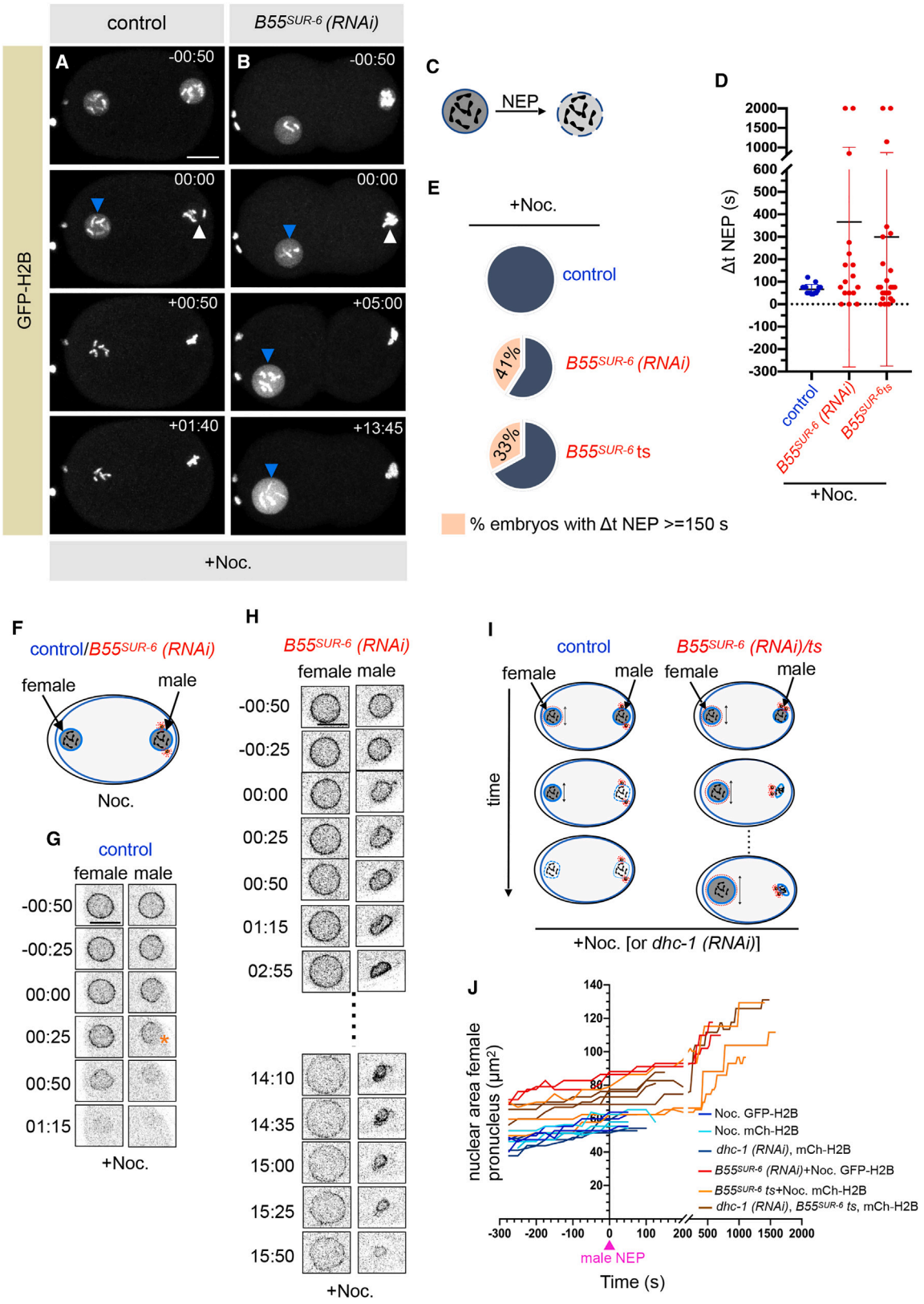

(legend on next page)

is regulated by active Aurora A, remains unchanged in B55^{SUR-6}-depleted embryos (Figures S1D–S1G).[32,47]

Transient accumulation of PLK-1 at the NE has been recently linked with NEBD.[13,14] Therefore, we tested the possibility of B55^{SUR-6} in regulating PLK-1 recruitment to the NE. However, we did not observe any significant change in the fluorescence intensity of PLK-1-sGFP either at the NE or at the centrosomes in B55^{SUR-6}-depleted embryos (Figures 2I–2N). Additionally, SPD-5 (a key protein involved in centrosome maturation) levels, which are regulated by active PLK-1, remain unchanged in B55^{SUR-6}-depleted embryos (Figures S2E, S2L–S2N).[48,49] These results are in line with our phenotypic observations that *B55^{SUR-6} (RNAi)* or *B55^{SUR-6}ts* embryos do not display any meiotic abnormality (data not shown), which is expected if B55^{SUR-6} would have been involved in controlling PLK-1 activity.[50] Altogether, these results indicate that B55^{SUR-6} has a direct role in promoting timely NEBD.

B55^{SUR-6} promotes the proper merging of parental genomes

Depletion or mutation in B55^{SUR-6} stabilizes nuclear lamina and a subset of NPPs. To assess if the stabilization of nuclear lamina/NPPs is sufficient to prevent the merging of parental genomes upon B55^{SUR-6} depletion, we utilized embryos expressing photoconvertible H2B (Dendra-H2B), photoconverted the male pronucleus before pronuclei meeting, and followed the fate of the genomes until the two-cell stage, as reported previously (Figure S3A).[11,15] The male and female genomes in control embryos, shown in magenta and green, are aligned on the metaphase plate. After segregation, the differently colored genomes are merged into a single nucleus at the two-cell stage (Figure S3B). In contrast, as expected, because of the improper NEBD, the male and the female genomes failed to merge in B55^{SUR-6}-depleted embryos (Figure S3C). These data indicate that B55^{SUR-6} is critical for intermixing of parental genomes.

Microtubule-dependent forces cooperate with B55^{SUR-6} for timely NEBD

Microtubules and NE-localized dynein/dynactin are proposed to generate mechanical tension on the NE for efficient NEBD in mammalian cells.[17,18] In the one-cell *C. elegans* embryo, when microtubules are depolymerized using Nocodazole or dynein activity is compromised, the male and female pronuclei fail to meet and undergo asynchronous NEP (Figures 3A and 3C; Video S3). In this setting, the male pronucleus undergoes permeabilization ~70 s before the female pronucleus (referred to as Δt NEP; Figure 3D).[7,8,10] Importantly, this asynchrony in NEP is independent of microtubules and dynein but dependent on Aurora A.[7,8] Since we uncovered that B55^{SUR-6} is essential for timely NEP and NEBD, we asked what happens to male and female pronuclei if the microtubules or dynein are compromised either in B55^{SUR-6}-depleted or *B55^{SUR-6}ts* embryos. Importantly, in ~40% of the embryos that were depleted for B55^{SUR-6} and treated with Nocodazole, the Δt NEP between the male and female pronuclei was above 150 s (Figures 3D and 3E); 150 s was chosen to emphasize extended asynchrony because this value is almost double the average Δt NEP that is seen for Nocodazole-treated control embryos. Intriguingly, ~15% of these embryos showed significantly extended asynchrony with Δt NEP of more than 700 s (Figures 3B and 3D; Video S4). Remarkably, we also noted that the chromosomes in the female pronucleus remained condensed for the entire duration of the time-lapse recording in this subset of embryos (Figure 3B; Video S4). Identical findings were obtained for *B55^{SUR-6}ts* embryos that were depleted for dynein (Figures S4A–S4E).

Since NEP is closely followed by the collapse of the spherical nuclear architecture, we sought to dissect the nuclear morphology in these settings. To this end, we performed time-lapse confocal imaging of Nocodazole-treated control and B55^{SUR-6}-depleted embryos expressing NPP-1-GFP. In Nocodazole-treated control embryos, the NE of male and female pronuclei is initially demarcated by a homogeneous fluorescence intensity of NPP-1-GFP. Here, the male pronucleus crumples ~70 s before the female pronucleus, followed by disappearance of the NPP-1-GFP signal (Figures 3F and 3G). In B55^{SUR-6}-depleted embryos with compromised microtubules, the male pronucleus shows crumpling of the NE; however, as expected, the NPP-1-GFP signal persisted given our observation on the role of B55^{SUR-6} in NE disassembly (Figures 3F and 3H). Strikingly, the female pronucleus that does not carry centrosomes and is far away from the male pronucleus shows a remarkably roundish NE that lasts for more than 150 s in ~40% of the

Figure 3. Microtubule-based forces synergize with B55^{SUR-6} for efficient NE disassembly

(A and B) Images from the time-lapse confocal microscopy of Nocodazole (Noc.)-treated control (A) and *B55^{SUR-6} (RNAi)* (B) embryos expressing GFP-H2B. Times are with respect to NEP of the male pronucleus (white arrowhead). Female pronucleus is shown by blue arrowhead. The scale bar in this and the following panels is 10 μm.

(C) Schematic depicting NEP as the loss of the nucleoplasmic H2B signal.

(D) Quantification of the difference in permeabilization (in s) between male and female pronuclei (Δt NEP) in Noc.-treated control (blue circles) or *B55^{SUR-6} (RNAi)*/*B55^{SUR-6}ts* (red circles) embryos. Note the tight window of data points from Noc.-treated control dataset (blue circles) with an average Δt NEP of ~70 s (66 ± 22 s, n = 15) in contrast to widespread data points in Noc.-treated B55^{SUR-6}-depleted (n = 17; red circles)/*B55^{SUR-6}ts* (n = 24; red circles) embryos. Error bars, SD.

(E) Pie chart depicting the pooled percentage of embryos showing asynchronous NEP (Δt NEP) in Noc.-treated control, *B55^{SUR-6} (RNAi)*, or *B55^{SUR-6}ts* embryos expressing GFP-H2B or mCherry-H2B and are in addition treated with Noc. [n = 7/17 for *B55^{SUR-6} (RNAi)* + Noc. and 8/24 for *B55^{SUR-6}ts* + Noc.].

(F) Schematic of control and *B55^{SUR-6} (RNAi)* embryos treated with Noc. showing failure in pronuclear migration.

(G and H) Male and female nuclear insets from the control (G) and *B55^{SUR-6} (RNAi)* (H) embryos expressing NPP-1-GFP that are in addition treated with Noc., as indicated.

(I) Schematic for analyzing the female pronuclear size of Noc. or *dhc-1 (RNAi)*-treated control or *B55^{SUR-6} (RNAi)*/*B55^{SUR-6}ts* embryos that are in addition treated with Noc. or *dhc-1 (RNAi)*, as indicated.

(J) Individual trajectories of the female nuclear size (in μm^2) from selected Noc.-treated control, *dhc-1 (RNAi)* or *B55^{SUR-6} (RNAi)*/*B55^{SUR-6}ts* embryos that are either treated with Noc. or *dhc-1 (RNAi)*, as mentioned. Nuclear expansion trajectories of individual female pronucleus in these conditions embryos are aligned with respect to male NEP (t = 0) (see STAR Methods).

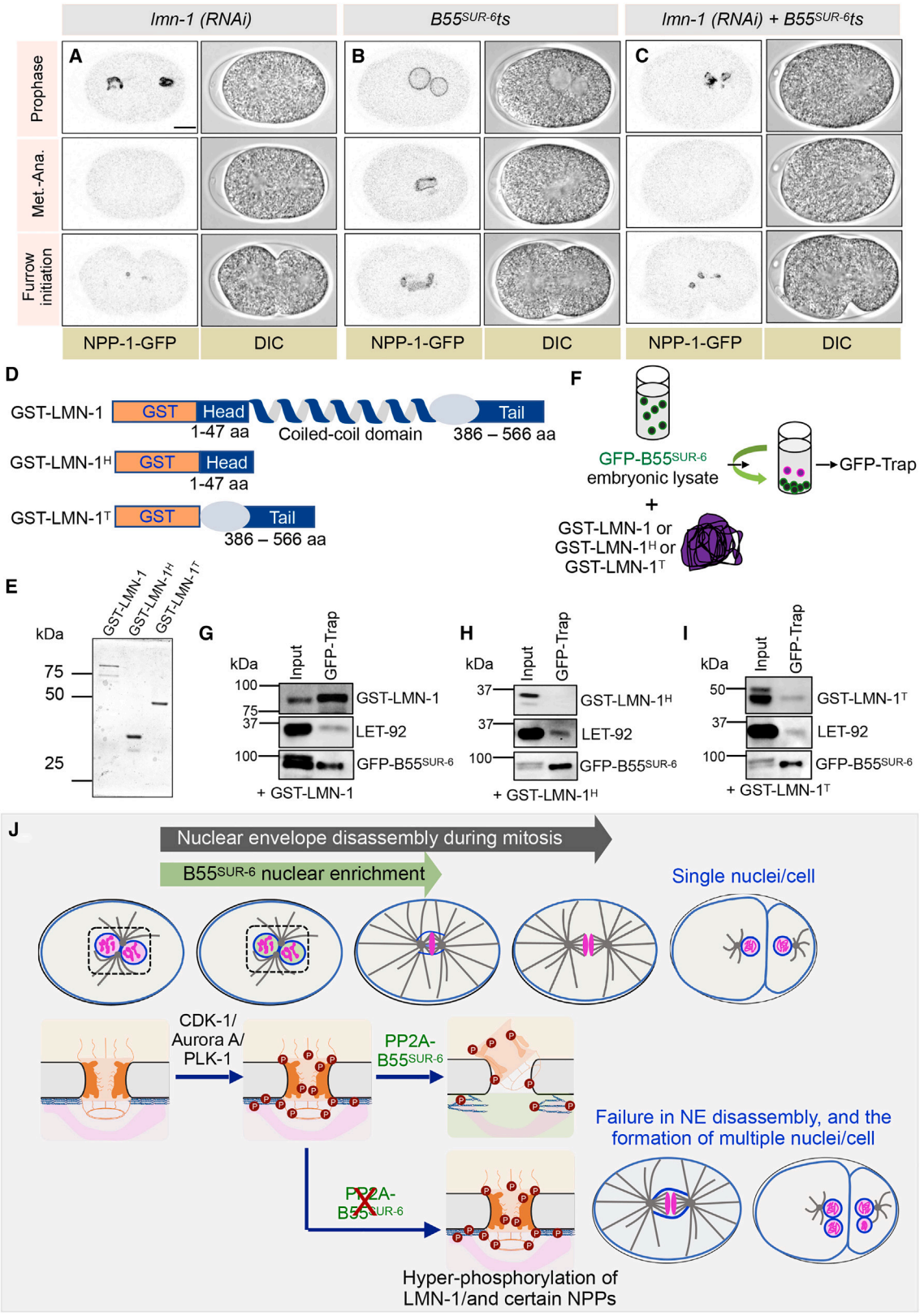

(legend on next page)

embryos (Figures 3E and 3H), and in 15% of these embryos, the female pronucleus stays roundish and continues to grow for a substantially longer duration of ~700 s or more (Figures 3H, 3I, and 3J). Similarly, *B55^{SUR-6}ts* embryos that are depleted of dynein preserve the spherical morphology of the female pronucleus for a significantly longer duration than the dynein-depleted control embryos (Figures 3J, S4A, and S4B; Videos S5 and S6). Altogether, these data suggest that microtubule-dependent forces, which alone are insufficient for NEBD, act synergistically with the B55^{SUR-6} for efficient NE disassembly in *C. elegans* embryos.

B55^{SUR-6} is robustly localized to the nucleus at NEP

To link B55^{SUR-6} role in NEBD with its localization, we utilized embryos coexpressing endogenous-tagged B55^{SUR-6} with GFP and FLAG tag (referred to as GFP-B55^{SUR-6})[51] and mCherry-tubulin. Time-lapse imaging of this line revealed that GFP-B55^{SUR-6} is enriched in both pronuclei during prophase (Figure S5A). During NEP, the nuclear GFP-B55^{SUR-6} levels are significantly enriched concomitant with the entry of free mCherry-tubulin signal from the cytoplasm (Figures S5A–S5C; Video S7). Further, to test if the nuclear enrichment of GFP-B55^{SUR-6} either at or a few seconds before NEP could be linked with NEBD, we analyzed the localization of GFP-B55^{SUR-6} in Nocodazole-treated embryos where male and female pronuclei undergo asynchronous NEP (Figure 3). As expected, the GFP-B55^{SUR-6} signal is nuclear during prophase. However, the GFP-B55^{SUR-6} fluorescence intensity is significantly enriched inside the male pronucleus ~50 s before the NEP of the female pronucleus (Figures S5D and S5E; Video S8). These observations together with the previous work that reported the localization of PP2A catalytical subunit, LET-92 in the pronuclei at or a few seconds before NEP,[52] raise a tempting possibility that the nuclear enrichment of the PP2A-B55^{SUR-6} complex promotes efficient NE permeabilization and its disassembly (see discussion).

LMN-1 is a potential target of B55^{SUR-6}

Hyper-phosphorylation of the lamin and nucleoporins by mitotic kinases drives NEBD.[5,9,15,53–56] It has been proposed that efficient nuclear disassembly might require the removal of the interphase phosphorylation marks from the lamin and nucleoporins.[56] However, to the best of our knowledge, no report shows if this occurs *in vivo*. We reasoned if PP2A-B55^{SUR-6} functions as a critical phosphatase required to remove certain inhibitory phosphate group/s from NPP/s or LMN-1 for NEBD, then the simultaneous depletion of B55^{SUR-6} with its substrate NPP/s or LMN-1 should rescue the NEBD defect seen in B55^{SUR-6}-depleted embryos (Figure S6A). To explore this, we performed a candidate-based RNAi suppressor screen by depleting B55^{SUR-6} along with various NPPs or LMN-1. RNAi-mediated depletion of 22 NPPs out of a total of 27[1] failed to disassemble the NPP-1-GFP signal seen in B55^{SUR-6}-depleted embryos (Table S1).

Next, we assessed the impact of LMN-1 depletion on NEBD in control or *B55^{SUR-6}ts* embryos expressing NPP-1-GFP. LMN-1 depletion impacts the nuclear morphology, as indicated previously; however, LMN-1 depletion had no impact on NE dissolution (Figure 4A).[37] In stark contrast with *B55^{SUR-6}ts* embryos, where the NPP-1-GFP nuclear signal persists in 100% of embryos (Figures 4B and S6B), depletion of LMN-1 in *B55^{SUR-6}ts* embryos resulted in the complete disappearance of the NPP-1-GFP signal in ~80% of the embryos (Figures 4C and S6B). We further validated these findings in the *C. elegans* strain expressing another nucleoporin marker GFP-NPP-19 (Figure S6B). Since the persistent nuclei observed in *B55^{SUR-6}ts* embryos disassembled upon LMN-1 depletion, we conclude that the lamina acts downstream of B55^{SUR-6} for timely NE dissolution.

To determine if LMN-1 could be a direct target of B55^{SUR-6}, we generated recombinant full-length LMN-1 with Glutathione S-transferase (GST) tag in *E. coli* (Figures 4D and 4E). Subsequently, we performed biochemical interaction studies by incubating GST-LMN-1 with the embryonic lysates from *C. elegans* strain expressing GFP-B55^{SUR-6} (Figure 4F). Co-immunoprecipitation (IP) with anti-GFP nanobody revealed that GFP-B55^{SUR-6} efficiently interacts with GST-LMN-1 and LET-92 (Figure 4G). Since LMN-1 disassembly is regulated by phosphorylation events at the LMN-1 head (1–47 aa) or tail (386–566 aa) domains,[15,56] we further generated recombinant LMN-1 head and

Figure 4. LMN-1 is a bona-fide target of B55^{SUR-6} for NEBD

(A–C) Images from time-lapse confocal microscopy in combination with DIC microscopy of embryos expressing NPP-1-GFP at various cell-cycle stages, as indicated in *lmn-1 (RNAi)* (A) in *B55^{SUR-6}ts* background (B) or *lmn-1 (RNAi)* in *B55^{SUR-6}ts* background (C). 100% of LMN-1-depleted embryos show complete disassembly of NPP-1-GFP signal (left panel), as opposed to 0% in *B55^{SUR-6}ts* embryos (middle panel). Note that 80% of LMN-1-depleted *B55^{SUR-6}ts* mutant embryos show disassembly of NPP-1-GFP signal [n = 30, *B55^{SUR-6}ts* mutant embryos; n = 7, *lmn-1 (RNAi)* embryos, and n = 10, *lmn-1 (RNAi)*, *B55^{SUR-6}ts* mutant embryos].

(D) Schematics of Glutathione S-transferase (GST)-tag LMN-1 (GST-LMN-1) or GST-tagged head domain (1–47 aa) of LMN-1 (GST-LMN-1^{H}), or GST-tagged tail domain (386–566 aa) of LMN-1 (GST-LMN-1^{T}).

(E) Coomassie-stained gel loaded with recombinant GST-LMN-1, GST-LMN-1^{H}, and GST-LMN-1^{T}.

(F) Schematic representation of the co-immunoprecipitation (IP) by GFP-Trap using embryonic lysate from embryos expressing GFP-B55^{SUR-6} after incubation with GST-LMN-1 or GST-LMN-1^{H} or GST-LMN-1^{T}.

(G–I) IP by GFP-Trap from embryonic lysates expressing GFP-B55^{SUR-6} that were incubated with GST-LMN-1 (G) or GST-LMN-1^{H} (H) or GST-LMN-1^{T} (I), as indicated (F). Resulting blots were probed for GST (to detect GST-tagged recombinant LMN-1 full length, or GST-LMN-1^{H}, or GST-LMN-1^{T}), LET-92 (the catalytic subunit), and FLAG (to detect GFP-B55^{SUR-6}). Input (2% of total), GFP-Trap fraction-33% of the total. Please note that 3% of IP fraction was loaded for the FLAG detection.

(J) Model for PP2A-B55^{SUR-6}-dependent NE disassembly pathway in *C. elegans* embryos. In control embryos, the nuclear localization and the rapid nuclear import of PP2A-B55^{SUR-6} at NEP (green) may help in erasing the inhibitory phosphorylation marks on the NE, including the lamina LMN-1, and NPPs. In the absence of PP2A-B55^{SUR-6}, hyperphosphorylation of some of the key residues prevents NE disassembly, leading to chromosome missegregation and the failure of merging of the parental genomes. In addition, our data suggest that microtubule-dependent forces, which alone are dispensable for NEBD onset, synergize with PP2A-B55^{SUR-6} for efficient NE disassembly.

tail domain fused to GST to analyze their interaction with GFP-B55^{SUR-6} (Figures 4D–4F). This analysis revealed that the C-terminal tail (GST-LMN-1^{T}), but not the head domain (GST-LMN-1^{H}), precipitates with the GFP-B55^{SUR-6} (Figures 4H and 4I). These results suggest that GFP-B55^{SUR-6} interacts with nuclear lamina component, LMN-1 and allude to an exciting possibility that PP2A-B55^{SUR-6} phosphatase activity might be required for dephosphorylation of some of the critical phosphorylated residues of the lamina for timely NE disassembly, and the merging of paternal and maternal genomes.

DISCUSSION

Disassembly of the NE is critical for proper chromosome segregation. How cells efficiently disassemble the NE comprising large complexes such as NPCs, lamina, and nucleoskeleton and cytoskeleton (LINC) linker during mitotic progression remains incompletely understood. Here, we discovered that an evolutionarily conserved PP2A regulatory subunit, B55^{SUR-6}, is vital for NEBD (Figure 4J).

B55^{SUR-6} is a crucial regulator of NEBD

B55^{SUR-6} promotes NEBD by facilitating lamina and nucleoporins disassembly. Failure of NEBD in B55^{SUR-6}-depleted one-cell embryos leads to the formation of more than one nucleus at the two-cell stage. This is most likely because of inefficient chromosomes capturing by the microtubules because of the physical barrier created by persistent NE, which causes inaccurate segregation of the chromosomes during anaphase and the formation of extra-nuclei. The inefficient chromosome capturing by the microtubules is seemingly not because of defective kinetochore organization or the microtubule emanation capacity of centrosomes.

How does B55^{SUR-6} regulate NEBD? A plethora of work has established that CDK-1, Aurora A, and PLK-1 facilitate NEBD in *C. elegans* embryos.[7,8,10,11,13,15,16,41,42] Therefore, one plausibility was that B55^{SUR-6} indirectly promotes NEBD by controlling the localization/activity of these kinases. However, the interval between meiosis completion to pseudocleavage regression/pronuclei meeting, which serves as phenotypic markers of the mitotic entry, remains unaltered upon B55^{SUR-6} depletion. This indicates that the mitotic onset, which chiefly relies on global CDK-1 activation, remains unaffected in B55^{SUR-6}-depleted embryos. Likewise, the downstream targets of Aurora A and PLK-1 remain unperturbed upon B55^{SUR-6} depletion, suggesting that the role of B55^{SUR-6} in NEBD is not possibly via regulating these kinases.

Our genetic analysis reveals that B55^{SUR-6} acts upstream of LMN-1, since the depletion of LMN-1 in either *B55^{SUR-6}ts* or B55^{SUR-6}-depleted embryos dissolves the NE. Furthermore, our biochemical interaction analysis revealed that B55^{SUR-6}, in complex with the PP2A catalytical subunit, LET-92 interacts with the globular tail domain of LMN-1. Given that the phosphorylation of the head and the tail domain of LMN-1 promotes its disassembly during mitosis,[15] we speculate that dephosphorylation of certain phosphorylated residues of LMN-1 by PP2A-B55^{SUR-6} complex could be a decisive step for timely NEBD (Figure 4J). In B55^{SUR-6}-depleted embryos, the LMN-1 would remain phosphorylated at those residues, creating a roadblock for NE disassembly (Figure 4J).

Microtubule and dynein-based forces cooperate with B55^{SUR-6} to initiate NEBD

In mammalian cells, microtubules and dynein-mediated mechanical forces are implicated in tearing down the NE.[17,18] Interestingly, microtubules and dynein are dispensable for NEBD in *C. elegans* embryos. This was beautifully demonstrated in conditions where male and female pronuclei failed to meet because of reduced microtubule nucleation or dynein dysfunction.[7,8] In such experiments, the male pronucleus carrying the centrosome commences NEP ~70 s before the female pronucleus. The NEP asynchrony between male and female pronucleus was shown to be microtubules and dynein-independent but Aurora A-dependent, which is enriched at the centrosomes, and thus in proximity to the male pronucleus.[7,8] Here, by treating B55^{SUR-6}-depleted embryos with Nocodazole, we unexpectedly observed an exaggerated increase in NEP asynchrony between male and female pronucleus. Intriguingly, in a subset of embryos, the female pronucleus failed to undergo NEP for significantly longer duration (~700 s or more). In such embryos, the female pronucleus retains all the chromosomes in a condensed state and steadily increases in size. These data suggest that initial NEP and subsequently, NEBD are critical events for DNA decondensation and act as a timer to reset the nuclear size and volume. Analogous observations were made in *B55^{SUR-6}ts* mutant embryos that are depleted for dynein. While not all B55^{SUR-6}-depleted and microtubule/dynein-compromised embryos show this exaggerated asynchrony in NEP, we think that residual microtubules in Nocodazole-treated, and partial dynein activity in DHC-1-depleted embryos may account for this observation. Overall, this work, and a recent work[57] that implicated the function of dynein-dependent cortical pulling forces in the pronuclear envelopes scission[57] imply that mechanical forces, which alone are dispensable for NEBD in *C. elegans* embryos, act synergistically with cellular biochemical machinery for efficient NE disassembly.

PP2A-B55^{SUR-6}: A missing link for NEBD during embryogenesis

The kinetics and timing of lamina depolymerization vary across different species. For instance, in human somatic cells, NEBD occurs in prophase.[3,58] In contrast, in *C. elegans* and *Drosophila* embryos, the lamina stay partly intact during prophase and are only completely dismantled during the metaphase-to-anaphase transition.[7,8,10,34,59–61] We uncovered that B55^{SUR-6} is crucial for NEP in *C. elegans*. In embryos depleted of B55^{SUR-6}, the NEP is significantly delayed by ~120 s, which is ~50% of the time that embryos spent from NEP to anaphase onset. Remarkably, NEP in *C. elegans* embryos coincides with the downfall in cyclin B levels and possibly with a decrease in CDK-1 activity that occurs ~200 s before metaphase-to-anaphase transition.[62] Since CDK-1/cyclinB-mediated phosphorylation is linked to cell-cycle-dependent regulation of PP2A-B55 in human cells,[22,63,64] we hypothesize that the decrease in CDK-1 activity at the NEP would be a decisive step in controlling PP2A-B55^{SUR-6} activity, and thus for the initiation of NEP and complete disassembly of the NE. Notably, since B55^{SUR-6} and its catalytic subunit LET-92[52] are enriched in the nucleoplasm, we envisage that the nuclear localization of the PP2A-B55^{SUR-6} holoenzyme in the one-cell

embryos makes this complex competent to carry out time-dependent NE disassembly in *C. elegans* and possibly in other species. In summary, our findings link the role of the PP2A-B55^{SUR-6} complex in NE disassembly and suggest the possibility of a biochemical cross-talk between kinases and phosphatase/s to choreograph NEBD.

Limitations of the study

Our data suggest that LMN-1 is the target of B55^{SUR-6}. However, which amino acid residue, or residues, of LMN-1 is the dephosphorylated by PP2A-B55^{SUR-6} remains unknown. Furthermore, genetic suppressor screen suggests that nucleoporins do not epistatically interact with B55^{SUR-6}; however, at this moment, we cannot firmly rule out a possibility that more than one nucleoporin could be a biochemical target of PP2A-B55^{SUR-6}. Future studies involving extensive biochemical characterization of B55^{SUR-6} targets in combination with phosphoproteomics analysis will shed light on the molecular mechanisms of PP2A-B55^{SUR-6}-mediated NE disassembly.

STAR★METHODS

Detailed methods are provided in the online version of this paper and include the following:

- KEY RESOURCES TABLE
- RESOURCE AVAILABILITY
  - Lead contact
  - Materials availability
  - Data and code availability
- EXPERIMENTAL MODEL AND STUDY PARTICIPANT DETAILS
- METHOD DETAILS
  - Drug treatment
  - RNAi
  - Time-lapse microscopy
  - Indirect immunofluorescence
  - Photoconversion experiment
  - Biochemical assays
- QUANTIFICATION AND STATISTICAL ANALYSIS
  - Assigning time '0'
  - Quantification of LMN-1 fluorescence intensity on the NE
  - Quantification of GFP and mCherry fluorescence intensity in GFP-tubulin, mCherry-TBG-1, GFP-AIR-1, mCherry-ZYG-9 and PLK-1-sGFP expressing embryos
  - Quantification of KNL-1 and MEL-28 intensity at the kinetochore
  - Quantification of nuclear fluorescence intensity for GFP-B55^{SUR-6} and mCherry-tubulin nuclear enrichment
  - Chromosome condensation kinetics

SUPPLEMENTAL INFORMATION

Supplemental information can be found online at https://doi.org/10.1016/j.celrep.2023.113495.

ACKNOWLEDGMENTS

We thank Arshad Desai, Lionel Pintard, Federico Pelisch, Sudha Kumari, and Caenorhabditis Genetics Center (CGC) for sharing reagents and worm strains. We are grateful to Arshad Desai, Lionel Pintard, Griselda Velez-Aguilera, Batool Ossareh-Nazari, Martin Lowe, Andrew Goryachev, and K. Subramaniam for their suggestions on the manuscript. We thank DST-FIST, UGC Center for the Advanced Study, Department of Biotechnology-Indian Institute of Science (DBT-IISc) Partnership Program, and IISc for the infrastructure support. This work is supported by the DBT grant (BT/PR36084/BRB/10/1857/2020), and DBT/Wellcome Trust India Alliance Fellowship (IA/I/15/2/502077) to S. Kotak.

AUTHOR CONTRIBUTIONS

S. Kapoor and S. Kotak initiated the project; S. Kapoor performed the experiments; S. Kapoor and K.A. generated *C. elegans* strains used for the experiments; S. Kotak wrote the original draft of the manuscript; S. Kotak and S. Kapoor did review and editing based on the inputs from the readers.

DECLARATION OF INTERESTS

The authors declare no competing interests.

INCLUSION AND DIVERSITY

We support inclusive, diverse, and equitable conduct of research.

Received: May 31, 2023
Revised: September 25, 2023
Accepted: November 9, 2023
Published: November 22, 2023

REFERENCES

1. Cohen-Fix, O., and Askjaer, P. (2017). Cell Biology of the Caenorhabditis elegans Nucleus. Genetics *205*, 25–59.
2. Pintard, L., and Bowerman, B. (2019). Mitotic Cell Division in Caenorhabditis elegans. Genetics *211*, 35–73.
3. Ungricht, R., and Kutay, U. (2017). Mechanisms and functions of nuclear envelope remodelling. Nat. Rev. Mol. Cell Biol. *18*, 229–245.
4. Kutay, U., Jühlen, R., and Antonin, W. (2021). Mitotic disassembly and reassembly of nuclear pore complexes. Trends Cell Biol. *31*, 1019–1033.
5. Heald, R., and McKeon, F. (1990). Mutations of phosphorylation sites in lamin A that prevent nuclear lamina disassembly in mitosis. Cell *61*, 579–589.
6. Peter, M., Nakagawa, J., Dorée, M., Labbé, J.C., and Nigg, E.A. (1990). In vitro disassembly of the nuclear lamina and M phase-specific phosphorylation of lamins by cdc2 kinase. Cell *61*, 591–602.
7. Portier, N., Audhya, A., Maddox, P.S., Green, R.A., Dammermann, A., Desai, A., and Oegema, K. (2007). A Microtubule-Independent Role for Centrosomes and Aurora A in Nuclear Envelope Breakdown. Dev. Cell *12*, 515–529.
8. Hachet, V., Canard, C., and Gönczy, P. (2007). Centrosomes Promote Timely Mitotic Entry in C. elegans Embryos. Dev. Cell *12*, 531–541.
9. Laurell, E., Beck, K., Krupina, K., Theerthagiri, G., Bodenmiller, B., Horvath, P., Aebersold, R., Antonin, W., and Kutay, U. (2011). Phosphorylation of Nup98 by multiple kinases is crucial for NPC disassembly during mitotic entry. Cell *144*, 539–550.
10. Hachet, V., Busso, C., Toya, M., Sugimoto, A., Askjaer, P., and Gönczy, P. (2012). The nucleoporin Nup205/NPP-3 is lost near centrosomes at mitotic onset and can modulate the timing of this process in Caenorhabditis elegans embryos. Mol. Biol. Cell *23*, 3111–3121.
11. Rahman, M.M., Munzig, M., Kaneshiro, K., Lee, B., Strome, S., Müller-Reichert, T., and Cohen-Fix, O. (2015). Caenorhabditis elegans polo-like

kinase PLK-1 is required for merging parental genomes into a single nucleus. Mol. Biol. Cell *26*, 4718–4735.

12. Solc, P., Kitajima, T.S., Yoshida, S., Brzakova, A., Kaido, M., Baran, V., Mayer, A., Samalova, P., Motlik, J., and Ellenberg, J. (2015). Multiple requirements of PLK1 during mouse oocyte maturation. PLoS One *10*, e0116783.
13. Martino, L., Morchoisne-Bolhy, S., Cheerambathur, D.K., Van Hove, L., Dumont, J., Joly, N., Desai, A., Doye, V., and Pintard, L. (2017). Channel Nucleoporins Recruit PLK-1 to Nuclear Pore Complexes to Direct Nuclear Envelope Breakdown in C. elegans. Dev. Cell *43*, 157–171.e7.
14. Linder, M.I., Köhler, M., Boersema, P., Weberruss, M., Wandke, C., Marino, J., Ashiono, C., Picotti, P., Antonin, W., and Kutay, U. (2017). Mitotic Disassembly of Nuclear Pore Complexes Involves CDK1- and PLK1-Mediated Phosphorylation of Key Interconnecting Nucleoporins. Dev. Cell *43*, 141–156.e7.
15. Velez-Aguilera, G., Nkombo Nkoula, S., Ossareh-Nazari, B., Link, J., Paouneskou, D., Van Hove, L., Joly, N., Tavernier, N., Verbavatz, J.-M., Jantsch, V., and Pintard, L. (2020). PLK-1 promotes the merger of the parental genome into a single nucleus by triggering lamina disassembly. Elife *9*, e59510–e59531.
16. Nkombo Nkoula, S., Velez-Aguilera, G., Ossareh-Nazari, B., Van Hove, L., Ayuso, C., Legros, V., Chevreux, G., Thomas, L., Seydoux, G., Askjaer, P., and Pintard, L. (2023). Mechanisms of nuclear pore complex disassembly by the mitotic Polo-like kinase 1 (PLK-1) in C. elegans embryos. Sci. Adv. *9*, eadf7826.
17. Beaudouin, J., Gerlich, D., Daigle, N., Eils, R., and Ellenberg, J. (2002). Nuclear envelope breakdown proceeds by microtubule-induced tearing of the lamina. Cell *108*, 83–96.
18. Salina, D., Bodoor, K., Eckley, D.M., Schroer, T.A., Rattner, J.B., and Burke, B. (2002). Cytoplasmic dynein as a facilitator of nuclear envelope breakdown. Cell *108*, 97–107.
19. Barr, F.A., Elliott, P.R., and Gruneberg, U. (2011). Protein phosphatases and the regulation of mitosis. J. Cell Sci. *124*, 2323–2334.
20. Gelens, L., Qian, J., Bollen, M., and Saurin, A.T. (2018). The Importance of Kinase–Phosphatase Integration: Lessons from Mitosis. Trends Cell Biol. *28*, 6–21.
21. Moura, M., and Conde, C. (2019). Phosphatases in Mitosis: Roles and Regulation. Biomolecules *9*, 55.
22. Nilsson, J. (2019). Protein phosphatases in the regulation of mitosis. J. Cell Biol. *218*, 395–409.
23. Foley, E.A., Maldonado, M., and Kapoor, T.M. (2011). Formation of stable attachments between kinetochores and microtubules depends on the B56-PP2A phosphatase. Nat. Cell Biol. *13*, 1265–1271.
24. Kruse, T., Zhang, G., Larsen, M.S.Y., Lischetti, T., Streicher, W., Kragh Nielsen, T., Bjørn, S.P., and Nilsson, J. (2013). Direct binding between BubR1 and B56-PP2A phosphatase complexes regulate mitotic progression. J. Cell Sci. *126*, 1086–1092.
25. Suijkerbuijk, S.J.E., Vleugel, M., Teixeira, A., and Kops, G.J.P.L. (2012). Integration of Kinase and Phosphatase Activities by BUBR1 Ensures Formation of Stable Kinetochore-Microtubule Attachments. Dev. Cell *23*, 745–755.
26. Kotak, S., Busso, C., and Gönczy, P. (2013). NuMA phosphorylation by CDK1 couples mitotic progression with cortical dynein function. EMBO J. *32*, 2517–2529.
27. Cundell, M.J., Bastos, R.N., Zhang, T., Holder, J., Gruneberg, U., Novak, B., and Barr, F.A. (2013). The BEG (PP2A-B55/ENSA/Greatwall) Pathway Ensures Cytokinesis follows Chromosome Separation. Mol. Cell *52*, 393–405.
28. Enos, S.J., Dressler, M., Gomes, B.F., Hyman, A.A., and Woodruff, J.B. (2018). Phosphatase PP2A and microtubule-mediated pulling forces disassemble centrosomes during mitotic exit. Biol. Open *7*. bio029777-9.
29. Keshri, R., Rajeevan, A., and Kotak, S. (2020). PP2A-B55γ counteracts Cdk1 and regulates proper spindle orientation through cortical dynein adaptor NuMA. J. Cell Sci. *133*, jcs243857.
30. O'Rourke, S.M., Carter, C., Carter, L., Christensen, S.N., Jones, M.P., Nash, B., Price, M.H., Turnbull, D.W., Garner, A.R., Hamill, D.R., et al. (2011). A survey of new temperature-sensitive, embryonic-lethal mutations in C. elegans: 24 alleles of thirteen genes. PLoS One *6*, e16644.
31. Cheeseman, I.M., Niessen, S., Anderson, S., Hyndman, F., Yates, J.R., Oegema, K., and Desai, A. (2004). A conserved protein network controls assembly of the outer kinetochore and its ability to sustain tension. Genes Dev. *18*, 2255–2268.
32. Kapoor, S., and Kotak, S. (2019). Centrosome Aurora A regulates RhoGEF ECT-2 localisation and ensures a single PAR-2 polarity axis in C. elegans embryos. Development *146*, dev174565.
33. Galy, V., Askjaer, P., Franz, C., López-Iglesias, C., and Mattaj, I.W. (2006). MEL-28, a Novel Nuclear-Envelope and Kinetochore Protein Essential for Zygotic Nuclear-Envelope Assembly in C. elegans. Curr. Biol. *16*, 1748–1756.
34. Askjaer, P., Galy, V., Hannak, E., and Mattaj, I.W. (2002). Ran GTPase Cycle and Importins α and β Are Essential for Spindle Formation and Nuclear Envelope Assembly in Living Caenorhabditis elegans Embryos. Mol. Biol. Cell *13*, 4355–4370.
35. Gorjánácz, M., Klerkx, E.P.F., Galy, V., Santarella, R., López-Iglesias, C., Askjaer, P., and Mattaj, I.W. (2007). Caenorhabditis elegans BAF-1 and its kinase VRK-1 participate directly in post-mitotic nuclear envelope assembly. EMBO J. *26*, 132–143.
36. Riemer, D., Dodemont, H., and Weber, K. (1993). A nuclear lamin of the nematode Caenorhabditis elegans with unusual structural features; cDNA cloning and gene organization. Eur. J. Cell Biol. *62*, 214–223.
37. Liu, J., Rolef Ben-Shahar, T., Riemer, D., Treinin, M., Spann, P., Weber, K., Fire, A., and Gruenbaum, Y. (2000). Essential Roles for Caenorhabditis elegans Lamin Gene in Nuclear Organization, Cell Cycle Progression, and Spatial Organization of Nuclear Pore Complexes. Mol. Biol. Cell *11*, 3937–3947.
38. Boudreau, V., Chen, R., Edwards, A., Sulaimain, M., and Maddox, P.S. (2019). PP2A-B55/SUR-6 collaborates with the nuclear lamina for centrosome separation during mitotic entry. Mol. Biol. Cell *30*, 876–886.
39. Aris, J.P., and Blobel, G. (1989). Yeast nuclear envelope proteins cross react with an antibody against mammalian pore complex proteins. J. Cell Biol. *108*, 2059–2067.
40. Galy, V., Mattaj, I.W., and Askjaer, P. (2003). Caenorhabditis elegans Nucleoporins Nup93 and Nup205 Determine the Limit of Nuclear Pore Complex Size Exclusion In Vivo. Mol. Biol. Cell *14*, 5104–5115.
41. Boxem, M., Srinivasan, D.G., and Van Den Heuvel, S. (1999). The Caenorhabditis elegans gene ncc-1 encodes a cdc2-related kinase required for M phase in meiotic and mitotic cell divisions, but not for S phase. Development *126*, 2227–2239.
42. van der Voet, M., Lorson, M.A., Srinivasan, D.G., Bennett, K.L., and van den Heuvel, S. (2009). C. elegans mitotic cyclins have distinct as well as overlapping functions in chromosome segregation. Cell Cycle *8*, 4091–4102.
43. Maddox, P.S., Portier, N., Desai, A., and Oegema, K. (2006). Molecular analysis of mitotic chromosome condensation using a quantitative time-resolved flourescence microscopy assay. Proc. Natl. Acad. Sci. USA *103*, 15097–15102.
44. Terasaki, M., Campagnola, P., Rolls, M.M., Stein, P.A., Ellenberg, J., Hinkle, B., and Slepchenko, B. (2001). A new model for nuclear envelope breakdown. Mol. Biol. Cell *12*, 503–510.
45. Lénárt, P., Rabut, G., Daigle, N., Hand, A.R., Terasaki, M., and Ellenberg, J. (2003). Nuclear envelope breakdown in starfish oocytes proceeds by partial NPC disassembly followed by a rapidly spreading fenestration of nuclear membranes. J. Cell Biol. *160*, 1055–1068.

46. Citi, S., and Kendrick-Jones, J. (1987). Regulation of non-muscle myosin structure and function. Bioessays *7*, 155–159.

47. Hannak, E., Kirkham, M., Hyman, A.A., and Oegema, K. (2001). Aurora-A kinase is required for centrosome maturation in Caenorhabditis elegans. J. Cell Biol. *155*, 1109–1116.

48. Woodruff, J.B., Wueseke, O., Viscardi, V., Mahamid, J., Ochoa, S.D., Bunkenborg, J., Widlund, P.O., Pozniakovsky, A., Zanin, E., Bahmanyar, S., et al. (2015). Regulated assembly of a supramolecular centrosome scaffold in vitro. Science *348*, 808–812.

49. Ohta, M., Zhao, Z., Wu, D., Wang, S., Harrison, J.L., Gómez-Cavazos, J.S., Desai, A., and Oegema, K.F. (2021). Polo-like kinase 1 independently controls microtubule-nucleating capacity and size of the centrosome. J. Cell Biol. *220*, e202009083.

50. Chase, D., Serafinas, C., Ashcroft, N., Kosinski, M., Longo, D., Ferris, D.K., and Golden, A. (2000). The polo-like kinase PLK-1 is required for nuclear envelope breakdown and the completion of meiosis inCaenorhabditis elegans. genesis *26*, 26–41.

51. Bel Borja, L., Soubigou, F., Taylor, S.J.P., Fraguas Bringas, C., Budrewicz, J., Lara-Gonzalez, P., Sorensen Turpin, C.G., Bembenek, J.N., Cheerambathur, D.K., and Pelisch, F. (2020). BUB-1 targets PP2A:B56 to regulate chromosome congression during meiosis I in C. elegans oocytes. Elife *9*, e65307–e65327.

52. Schlaitz, A.-L., Srayko, M., Dammermann, A., Quintin, S., Wielsch, N., MacLeod, I., de Robillard, Q., Zinke, A., Yates, J.R., Müller-Reichert, T., et al. (2007). The C. elegans RSA Complex Localizes Protein Phosphatase 2A to Centrosomes and Regulates Mitotic Spindle Assembly. Cell *128*, 115–127.

53. Gerace, L., and Blobel, G. (1980). The nuclear envelope lamina is reversibly depolymerized during mitosis. Cell *19*, 277–287.

54. Mühlhäusser, P., and Kutay, U. (2007). An in vitro nuclear disassembly system reveals a role for the RanGTPase system and microtubule-dependent steps in nuclear envelope breakdown. J. Cell Biol. *178*, 595–610.

55. Mehsen, H., Boudreau, V., Garrido, D., Bourouh, M., Larouche, M., Maddox, P.S., Swan, A., and Archambault, V. (2018). PP2A-B55 promotes nuclear envelope reformation after mitosis in Drosophila. J. Cell Biol. *217*, 4106–4123.

56. Machowska, M., Piekarowicz, K., and Rzepecki, R. (2015). Regulation of lamin properties and functions: Does phosphorylation do it all? Open Biol. *5*, 150094.

57. Velez-Aguilera, G., Ossareh-Nazari, B., Van Hove, L., Joly, N., and Pintard, L. (2022). Cortical microtubule pulling forces contribute to the union of the parental genomes in the Caenorhabditis elegans zygote. Elife *11*, e75382.

58. Hetzer, M.W. (2010). The nuclear envelope. Cold Spring Harb. Perspect. Biol. *2*, a000539.

59. Paddy, M.R., Saumweber, H., Agard, D.A., and Sedat, J.W. (1996). Time-resolved, in vivo studies of mitotic spindle formation and nuclear lamina breakdown in Drosophila early embryos. J. Cell Sci. *109*, 591–607.

60. Lee, K.K., Gruenbaum, Y., Spann, P., Liu, J., and Wilson, K.L. (2000). C. elegans Nuclear Envelope Proteins Emerin, MAN1, Lamin, and Nucleoporins Reveal Unique Timing of Nuclear Envelope Breakdown during Mitosis. Mol. Biol. Cell *11*, 3089–3099.

61. Katsani, K.R., Karess, R.E., Dostatni, N., and Doye, V. (2008). In Vivo Dynamics of Drosophila Nuclear Envelope Components. Mol. Biol. Cell *19*, 3652–3666.

62. Kim, T., Lara-Gonzalez, P., Prevo, B., Meitinger, F., Cheerambathur, D.K., Oegema, K., and Desai, A. (2017). Kinetochores accelerate or delay APC/C activation by directing Cdc20 to opposing fates. Genes Dev. *31*, 1089–1094.

63. Schmitz, M.H.A., Held, M., Janssens, V., Hutchins, J.R.A., Hudecz, O., Ivanova, E., Goris, J., Trinkle-Mulcahy, L., Lamond, A.I., Poser, I., et al. (2010). Live-cell imaging RNAi screen identifies PP2A-B55α and importin-β 21 as key mitotic exit regulators in human cells. Nat. Cell Biol. *12*, 886–893.

64. Cundell, M.J., Hutter, L.H., Nunes Bastos, R., Poser, E., Holder, J., Mohammed, S., Novak, B., and Barr, F.A. (2016). A PP2A-B55 recognition signal controls substrate dephosphorylation kinetics during mitotic exit. J. Cell Biol. *214*, 539–554.

65. Golden, A., Liu, J., and Cohen-Fix, O. (2009). Inactivation of the C. elegans lipin homolog leads to ER disorganization and to defects in the breakdown and reassembly of the nuclear envelope. J. Cell Sci. *122*, 1970–1978.

66. Bolková, J., and Lanctôt, C. (2016). Live imaging reveals spatial separation of parental chromatin until the four-cell stage in Caenorhabditis elegans embryos. Int. J. Dev. Biol. *60*, 5–12.

67. Gómez-Saldivar, G., Fernandez, A., Hirano, Y., Mauro, M., Lai, A., Ayuso, C., Haraguchi, T., Hiraoka, Y., Piano, F., and Askjaer, P. (2016). Identification of Conserved MEL-28/ELYS Domains with Essential Roles in Nuclear Assembly and Chromosome Segregation. PLoS Genet. *12*, e1006131.

68. Voronina, E., and Seydoux, G. (2010). The C. elegans homolog of nucleoporin Nup98 is required for the integrity and function of germline P granules. Development *137*, 1441–1450.

69. Dickinson, D.J., Ward, J.D., Reiner, D.J., and Goldstein, B. (2013). Engineering the Caenorhabditis elegans genome using Cas9-triggered homologous recombination. Nat. Methods *10*, 1028–1034.

70. Toya, M., Iida, Y., and Sugimoto, A. (2010). Imaging of Mitotic Spindle Dynamics in Caenorhabditis elegans Embryos. In Methods in Cell Biology, pp. 359–372.

71. Bienkowska, D., and Cowan, C.R. (2012). Centrosomes Can Initiate a Polarity Axis from Any Position within One-Cell C. elegans Embryos. Curr. Biol. *22*, 583–589.

72. Boyd, L., Guo, S., Levitan, D., Stinchcomb, D.T., and Kemphues, K.J. (1996). PAR-2 is asymmetrically distributed and promotes association of P granules and PAR-1 with the cortex in C. elegans embryos. Development *122*, 3075–3084.

73. Johnston, W.L., Krizus, A., and Dennis, J.W. (2006). The eggshell is required for meiotic fidelity, polar-body extrusion and polarization of the C. elegans embryo. BMC Biol. *4*. 35-21.

74. Rual, J.-F., Ceron, J., Koreth, J., Hao, T., Nicot, A.-S., Hirozane-Kishikawa, T., Vandenhaute, J., Orkin, S.H., Hill, D.E., van den Heuvel, S., and Vidal, M. (2004). Toward Improving Caenorhabditis elegans Phenome Mapping With an ORFeome-Based RNAi Library. Genome Res. *14*, 2162–2168.

75. Kamath, R.S., Fraser, A.G., Dong, Y., Poulin, G., Durbin, R., Gotta, M., Kanapin, A., Le Bot, N., Moreno, S., Sohrmann, M., et al. (2003). Systematic functional analysis of the Caenorhabditis elegans genome using RNAi. Nature *421*, 231–237.

76. Gönczy, P., Schnabel, H., Kaletta, T., Amores, A.D., Hyman, T., and Schnabel, R. (1999). Dissection of cell division processes in the one cell stage Caenorhabditis elegans embryo by mutational analysis. J. Cell Biol. *144*, 927–946.

77. Rosu, S., and Cohen-Fix, O. (2017). Live-imaging analysis of germ cell proliferation in the C. elegans adult supports a stochastic model for stem cell proliferation. Dev. Biol. *423*, 93–100.

78. Dumont, J., Oegema, K., and Desai, A. (2010). A kinetochore-independent mechanism drives anaphase chromosome separation during acentrosomal meiosis. Nat. Cell Biol. *12*, 894–901.

STAR★METHODS

KEY RESOURCES TABLE

REAGENT or RESOURCE	SOURCE	IDENTIFIER
Antibodies		
Primary: Anti-GST	Sigma-Aldrich	Cat# G7781; RRID:AB_259965
Primary: Anti-FLAG	Sigma-Aldrich	Cat# F7425; RRID:AB_439687
Primary: PP2A C	Cell Signaling Technology	Cat# 2038; RRID:AB_2169495
Primary: mAB414	BioLegend	Cat# 902907; RRID:AB_2734672
Secondary: Alexa 488-conjugated anti-mouse	Molecular Probes	Cat# A-11008; RRID:AB_143165
Secondary: Goat anti-Rabbit IgG antibody, HRP conjugate	Sigma-Aldrich	Cat# 12–348; RRID:AB_390191
Bacterial and virus strains		
E. coli: HT115(DE3) [E. coli [F-, mcrA, mcrB, IN(rrnD-rrnE)1, rnc14:Tn10(DE3 lysogen: lacUV5 promoter -T7 polymerase]]	Caenorhabditis Genetics Center (CGC)	HT115 (DE3)
E. coli: OP50: E. coli B, uracil auxotroph	CGC	OP50
See Table S1 for list of genes used for feeding RNAi		
Chemicals, peptides, and recombinant proteins		
GFP-Trap agarose beads	ChromoTek	Cat# GTA-20; ACT-CM-GF A0050
Dextran tetramethylrhodamine 70,000 MW, lysine fixable	Invitrogen	Cat# D1818
Lysozyme from chicken egg white	Sigma-Aldrich	Cat# L6876
Protease Inhibitor Cocktail Set III, EDTA-Free-Calbiochem	Merck Millipore	Cat# 539134
Glycerol	Sigma-Aldrich	Cat# G5516
Imidazole	Sigma-Aldrich	Cat# I-2399
Nitrocellulose membrane	Bio-Rad	Cat# 1620115
BSA	HiMedia	Cat# MB083
Skimmed milk	HiMedia	Cat# GRM1254
2-mercaptoethanol	Sigma-Aldrich	Cat# M3148
DTT (Dithiothreitol)	ThermoFisher Scientific	Cat# R0861
Urea ACS	Merck Millipore	CAS# 57-13-6
HEPES	Sigma-Aldrich	Cat# H3375
Ni-NTA Agarose	Qiagen	Cat# 30230
30% Acrylamide/Bis Solution 29:1	Bio-Rad	Cat# 1610156
SDS	Qualigens, ThermoFisher Scientific	Cat# Q14136
Clarity Western ECL Substrate	Bio-Rad	Cat# 170-5060
Nocodazole	Sigma-Aldrich	Cat# M1404
Experimental models: Organisms/strains		
Wild type (*Caenorhabditis elegans*)	Caenorhabditis Genetics Center (CGC)	*C. elegans* N2 Bristol
GFP-B55^{SUR-6}	Arshad Desai; Bel Borja et al.[51]	OD4579
PLK-1-GFP; plk-1(lt17) [plk-1:sgfp]*loxP*)III	CGC; Martino et al.[13]	OD2425
YFP-LMN-1; mCherry-H2B; ltIs37 [pie-1p:mCherry: his-58 + unc-119(+)] IV. qaIs3502[pie-1:YFP:: LMN-1 + unc-119(+)]	CGC	OD139
NPP-1-GFP; mCherry-H2B; jjIs1092 [(pNUT1) npp-1:GFP + unc-119(+)]. ltIs37 [pie-1p: mCherry:his-58 + unc-119(+)] IV	CGC; Golden et al.[65]	OCF3

(*Continued on next page*)

Continued

REAGENT or RESOURCE	SOURCE	IDENTIFIER
GFP-H2B; mCherry-Emerin	KS Subramanium	it868
GFP-H2B; mCherry-SP12	KS Subramanium	it907
Dendra-2-his-58/66; ocfSi1 [mex-5p:Dendra2: his-58/66:tbb-2 3′UTR + unc-119(+)] I	CGC; Bolková and Lanctôt[66]	OCF69
GFP-MEL-28; mel-28(bq5[gfp:mel-28]) III	CGC; Gómez-Saldivar and Fernandez et al.[67]	BN426
GFP-NPP-9; axIs1595 [pie-1p:GFP:npp-9(orf): npp-9 3′UTR + unc-119(+)]	CGC; Voronina and Seydoux[68]	JH2184
GFP-NMY-2; cp13[nmy-2:gfp + *LoxP*] I	CGC; Dickinson et al.[69]	LP162
GFP-LEM-2; mCherry-H2B; ltIs37 [pie-1p: mCherry:his-58 + unc-119(+)] IV. qaIs3507 [pie-1:GFP:lem-2 + unc-119(+)]	CGC	OD83
GFP-NPP-19; bqIs7 [pie-1p:LAP:npp-19 + unc-119(+)]	CGC	BN46
GFP-KNL-3; ltIs1[pIC22; pie-1 promoter: knl-3:GFP + unc-119(+)]	CGC	OD1
GFP-B55^{SUR-6}; mCherry tubulin	This study	
B55^{SUR-6}ts (temperature-sensitive)	CGC; O'Rourke et al.[30]	EU1062
B55^{SUR-6}ts; NPP-1-GFP; mCherry H2B	This study	
B55^{SUR-6}ts; NPP-1-GFP; mCherry H2B; TagRFP SPD-5	This study	
GFP-AIR-1; mCherry-PAR-2	Kapoor and Kotak[32]	SK003
GFP-TBB-2; mCherry TBG-1; tjIs54 [pie-1p:GFP: tbb-2 + pie-1p:2xmCherry:tbg-1 + unc-119(+)]. tjIs57 [pie-1p:mCherry:his-48 + unc-119(+)]	Toya et al.[70]	SA250
mCherry-ZYG-9	Anthony A. Hyman	TH165
Oligonucleotides		
Feeding RNAi oligos (See Table S1)	Bioserve; https://www.reprocell.com/bioserve	N/A
Recombinant DNA		
L4440	http://www.addgene.org/1654	RRID:Addgene_1654
pETM30	https://grp-pepcore.embl-community.io/vectors/ecoli.html	EMBL expression vectors
Software and algorithms		
ImageJ/Fiji	http://fiji.sc/	RRID:SCR_002285
Imaris	http://www.bitplane.com/imaris/imaris	RRID:SCR_007370
GraphPad Prism	https://www.graphpad.com/	RRID:SCR_002798
MATLAB_R2020b	http://www.mathworks.com/products/matlab/	RRID:SCR_001622
SnapGene Viewer	http://www.snapgene.com/products/snapgene_viewer/	RRID:SCR_015053

RESOURCE AVAILABILITY

Lead contact

Further information and requests for resources and reagents should be directed to and will be fulfilled by the lead contact, Sachin Kotak (sachinkotak@iisc.ac.in).

Materials availability

Plasmids, protein and *C. elegans* strains generated during this study are freely available from the lead contact upon request.

Data and code availability

- Microscopy data reported in this paper will be shared by the lead contact upon request.

- This paper does not report original code.
- Any additional information required to reanalyze the data reported in this work is available from lead contact upon request.

EXPERIMENTAL MODEL AND STUDY PARTICIPANT DETAILS

C. elegans wild-type (N2) and transgenic lines expressing GFP/sGFP/mCherry/Tag RFP-tagged proteins were maintained at either 20°C or 24°C with Nematode Growth Media (NGM) plates seeded with *E. Coli* (OP50) or *E. Coli* (HT115) when performing RNAi, as a food source. Temperature-sensitive strains were maintained at 15°C. A list of all strains used in the study has been provided in key resources table. Many *C. elegans* strains were obtained from CGC, funded by the NIH Office of Research Infrastructure Programs (P40 OD010440).

METHOD DETAILS

Drug treatment

Microtubule poison Nocodazole treatment was performed as described.[32,71] In brief, worms were dissected in Nocodazole (10 μg/mL; Sigma Aldrich: M1404) containing egg buffer (118 mM NaCl, 40 mM KCl, 3.4 mM MgCl2, 3.4 mM CaCl2 and 5 mM HEPES pH 7.4; also see Boyd et al., 1996[72]) and the drug could enter in the embryos because of the permeability of the eggshell during meiosis II.[73] The efficiency of Nocodazole was determined by the inability of the male and female pronuclei to migrate.

RNAi

Bacterial RNAi feeding strains for B55^{SUR-6}, lmn-1, dhc-1, and several nucleoporins (NPPs) (Table S1) were obtained from the C. elegans ORFeome RNAi library[74] or Source BioScience.[75] Feeding vectors for a few NPPs (Table S1) were generated by amplifying the gene from either cDNA/gDNA and cloning in L4440 feeding vector (list of all NPPs used in screen provided in Table S1). RNAi against all the genes used in this work (see Table S1) was performed by feeding animals starting at the L2 or L3 stage with bacteria expressing the corresponding dsRNAs at 20°C or 24°C for 24–48 h before analysis. While performing double depletion using RNAi, the single depletion was performed side by side to observe the single RNAi-mediated phenotype.

RNAi experiments in *B55^{SUR-6}ts* mutant strain (EU1062) was performed by picking L3-L4 on RNAi feeding plate for 12–20 h at 15°C followed by shifting the feeding plates to the restrictive temperature of 25°C for 12–24 h, as in *dhc-1 (RNAi)* or *lmn-1 (RNAi)*.

Time-lapse microscopy

For recording embryos, gravid worms were dissected in M9 or egg buffer and transferred onto a 2% agarose pad containing slides using a mouth pipette. These were then covered with a 20 × 20 mm coverslip. Time-lapse Differential Interference Contrast (DIC) microscopy, Confocal microscopy in combination with DIC were performed on such embryos either on IX53 (Olympus Corporation, Japan) with Qimaging Micropublisher 5.0 Color CCD Camera (Qimaging, Canada) with 100X 1.4 NA objective, or FV3000 Confocal system with high-sensitivity cooled GaAsP detection unit (Olympus Corporation, Japan) using 60X 1.4 NA objective. Images were collected at intervals of 5–25 s per frame. Videos were subsequently processed using ImageJ maintaining relative image intensities within a series. z stack series were projected as maximum intensity projections for embryos expressing mCherry-ZYG-9, GFP-Aurora A, mCherry-H2B, GFP-KNL-3, GFP-MEL-28, and Dendra-H2B.

Indirect immunofluorescence

Embryo fixation and staining for indirect immunofluorescence was performed mostly as described[76] using 1:200 rabbit anti-mAB414 (Biolegend: 902907). Embryos were fixed in methanol at −20°C for 30 min and incubated with primary antibodies for 1 h at room temperature. Secondary antibodies were Alexa 488-coupled anti-mouse used at 1:500. Confocal images were acquired on an FV3000 Confocal system with high-sensitivity cooled GaAsP detection unit (Olympus Corporation, Japan) using 60× objective with NA 1.4 oil and processed in ImageJ and Adobe Photoshop, maintaining relative image intensities.

Photoconversion experiment

Photoconversion experiments of worms expressing photoconvertible histone, Dendra2-H2B (strain OCF69) were performed as described in Rosu and Cohen-Fix, 2017.[77] A circular ROI around the male pronucleus was illuminated with a 405 nm laser set at low power of 0.9% for 20 ms and pixel dwell time of 10 ms. This was done before pronuclear meeting. A green-to-red photoconversion of the labeled H2B chromosomes was observed, and the embryos were recorded using z-stacking with 1.5 μm with 25 s time interval as described before. Image stacks were processed using Fiji and are represented as maximum z-projections.

Biochemical assays

Purification of GST-tagged LMN-1, LMN-1^{H}, and LMN-1^{T} fragments

GST-LMN-1 was amplified from cDNA and cloned in pETM30 protein expression vector (6xHis-GST-TEV-LMN-1) and the purification was done as described.[15] Protein expression was induced with 1mM IPTG in 400 mL of BL21 DE3 pLysS strain at OD = 0.6–0.8, by incubation at 25°C for 3 h. Cells pellet was collected by centrifugation at 6000 rpm for 10 min, and the pellet was then suspended in

urea lysis buffer (8 M urea, 100 mM NaCl, 10 Mm Tris–HCl, pH 8, 1 mM 2-mercaptoethanol). Sonication was done at 30% amplitude, four times for 30 s each. Supernatant was collected after centrifugation at 11000 rpm for 30 min at room temperature. Purification was done using Ni-NTA (Qiagen: 30230) beads using gravity column, using binding buffer (8M Urea, 50mM Tris–HCl pH 8.0, 500mM NaCl, 20mM imidazole and 1 mM 2-mercaptoethanol). Beads were washed using wash buffer (8M Urea, 50mM Tris–HCl pH 8.0, 500mM NaCl, 40mM imidazole and 1 mM 2-mercaptoethanol). Elution was done in 8M urea, 10 mM Tris–HCl pH 8.0, 500mM imidazole, followed by stepwise dialysis to remove urea (10 mM Tris–HCl pH 8.0, 100 mM NaCl, 1 mM 2-mercaptoethanol). Protein dialysis was performed at 4°C and the protein was aliquoted and stored at −80°C after the snap freeze.

Likewise, LMN-1^H and LMN-1^T fragments were cloned in pETM30 protein expression vector (6xHis-GST-TEV-LMN-1^H and 6xHis-GST-TEV-LMN-1^T). Protein expression was induced with 1mM IPTG in 400 mL of BL21 DE3 pLys cells at OD = 0.6–0.8, by incubation at 25°C for 3 h. Cells pellet was collected by centrifugation at 5000 rpm for 20 min at 4°C and resuspended in lysis buffer (0.5M NaCl, 5% glycerol, 50mM Tris/HCl (pH = 8), and 1x protease inhibitor cocktail). Lysozyme (Sigma, 1.5 mg/mL) and DNase was added before sonication at 30% amplitude (3 s ON, 5 s OFF, 5 min). 0.5% Triton X- was added and the supernatant was collected after centrifugation at 13,000 rpm for 15 min at 4°C. For protein purification, the supernatant was incubated with NiNTA Beads (Qiagen: 30230) and 20mM Imidazole and kept at end-on rotation at 4°C. The supernatant was loaded on gravity column and washed with Wash Buffer (0.5M NaCl, 5% Glycerol, 50mM Tris-HCl (pH = 8), 1x protease inhibitor cocktail, 40mM Imidazole). Bound protein was eluted in elution buffer containing 500mM Imidazole (100mM NaCl, 5% Glycerol, 10mM Tris-HCl (pH = 8), and 1x protease inhibitor cocktail). Overnight protein dialysis (10 mM Tris–HCl pH 8.0, 100 mM NaCl, 1 mM 2-mercaptoethanol) was performed at 4°C and the protein was aliquoted and stored at −80°C after snap freeze.

GFP-trap experiments

2 mg equivalent embryonic lysate from worms expressing GFP-$B55^{SUR-6}$ was incubated with either 250 ng GST-LMN-1, or GST-LMN-1^H, or GST-LMN-1^T with 0.2 mM working concentration of ATP at room temperature for 15 min. This was done to allow phosphorylation or modification, if any, of exogenously produced bacterial protein with embryonic lysate. An aliquot was collected as input fraction after this brief incubation, and the remaining sample was incubated with 25 μl GFP-Trap beads (Chromotek: ACT-CM-GFA0050). Before incubation, GFP-Trap beads were washed thrice in 500 μl ice-cold dilution buffer (lysis buffer without Glycerol and NP40) with DTT (ThermoFisher Scientific: R0861) and PI (Merck: 539134) by spinning at 1000xg for 2 min. The beads were incubated with embryo lysate with GST-LMN-1, GST-LMN-1^H, or GST-LMN-1^T and kept for end-on rotation for 2–3 h at 4°C. The samples were spun at 2500xg for 2 min and the supernatant un-bound fraction was collected. 3 washes were done with dilution buffer followed by addition of 80 μl 2x SDS dye. The samples were boiled at 95°C for 10 min. The samples were spun at 2500xg for 5 min to collect the supernatant fraction, followed by immunoblotting.

Immunoblotting

For immunoblotting, the samples were loaded on 8% SDS gel and transferred onto the nitrocellulose membrane (Biorad: 1620115) for immunoblot analysis. Blocking was done in BSA (HiMedia: MB083), and incubation with primary antibodies was done overnight at 40C. Anti-GST (Sigma: G7781) at 1:1000 dilution prepared in 5% BSA was used to detect LMN-1 protein. GFP-$B55^{SUR-6}$ signal in the bead-bound fraction was detected using anti-FLAG (Sigma: F7425 Sigma) at 1:1000 prepared in 5% skimmed milk (HiMedia: GRM1254). Since LET-92 protein sequence is 88.67% identical to human PPP2CA, PP2A C (CST: 2038) antibodies were used to detect LET-92, which detects a single band on the SDS-PAGE at the right size, and this band disappears in let-92 (RNAi) condition (data not shown).

QUANTIFICATION AND STATISTICAL ANALYSIS

Fiji/ImageJ (https://fiji.sc/), Imaris (Bitplane Inc.), and GraphPad Prism were used to perform quantitative analysis. Fiji was used to quantify nuclear area using circular selection (Figures 3J and S1P). Imaris was used for 3D rendering of the nucleus and quantification of volume. The p value was considered to be significant if $p < 0.05$ using GraphPad Prism 8. The p values are either mentioned in text or on the graph and the significance values are mentioned as n.s., >0.05; *$p < 0.05$; **$p < 0.01$; ***$p < 0.001$.

Assigning time '0′

For most datasets and graphs, t = 0 corresponds to nuclear envelope permeabilization (NEP). This is the frame at which there is a visible exclusion of nucleoplasmic H2B signal or inclusion of tubulin signal. However, in the context of chromosome condensation kinetics (Figure 2D), nuclear size expansion-related graphs (Figure S1P) the pronuclear meeting timing is considered '0′ as indicated.

Quantification of LMN-1 fluorescence intensity on the NE

A fixed rectangular ROI (ROI of 2.4 μm^2) was placed on the nuclear envelope at the time intervals indicated on the graph on single z sections of the image. The integrated fluorescence intensity in this ROI and a similarly sized ROI in the cytoplasm and background were determined using Fiji/ImageJ. Fluorescence intensity at the Nuclear envelope and cytoplasm was subtracted from the background, and the ratio of NE/cytoplasm to indicate NE enrichment was used for plotting the graph. Signal intensities were compared using a two-sample unpaired t test in GraphPad Prism.

Quantification of GFP and mCherry fluorescence intensity in GFP-tubulin, mCherry-TBG-1, GFP-AIR-1, mCherry-ZYG-9 and PLK-1-sGFP expressing embryos

Centrosome intensity of GFP-tubulin (ROI of area 12.574 μm^2), mCherry-TBG-1 (ROI of area 12.875 μm^2), GFP-AIR-1 (ROI of area 28.67 μm^2), mCherry-ZYG-9 (ROI of area 9.27 μm^2) and PLK-1-sGFP (ROI of area 3.4 μm^2) expressing embryos was quantified by taking the ratios of fluorescent intensities at the centrosome w.r.t cytoplasm and corrected for the background. The nuclear envelope intensity of PLK-1-sGFP (ROI of area 2.96 μm^2) expressing embryos was also quantified with the method described above for LMN-1.

Quantification of KNL-1 and MEL-28 intensity at the kinetochore

Quantification of KNL-1 and MEL-28 kinetochore localization in GFP-KNL-1 and GFP-MEL-28 expressing embryos at the metaphase stage of one-cell embryos was performed on maximum intensity projections show in schematic in Figure S1J, as in Dumont et al., 2010.[78] In brief, a rectangular ROI was drawn around the kinetochore signal, and integrated pixel intensity was measured. The ROI was expanded by 5 pixels and the difference in the integrated intensity between this ROI and the original ROI was used to define the background. Integrated kinetochore fluorescence is calculated as the value of the original ROI after background subtraction. For data representation on plot, the values have been normalized to 1 with respect to the maximum kinetochore intensity observed in control values.

Quantification of nuclear fluorescence intensity for GFP-B55^{SUR-6} and mCherry-tubulin nuclear enrichment

A fixed circular ROI (area 3.4 μm^2) was placed manually inside the nucleus at time intervals indicated on the graph. The integrated fluorescence intensity in this ROI and a similarly sized ROI in the cytoplasm and background were determined using Fiji/ImageJ. Fluorescence intensity at the centrosome and cytoplasm was subtracted from the background, and the ratio of centrosome/cytoplasm was used for plotting the graph. Signal intensities were compared using a two-sample unpaired t test in GraphPad Prism.

Chromosome condensation kinetics

The kinetics was done as described in Maddox et al., 2006.[43] Worms expressing GFP-H2B were recorded with z-stacking at 1.5 μm step size and 9 sections. Maximum z-projection was done on Fiji, and a rectangular region of interest around the chromosomes was cropped and converted to an 8-bit scale [0:255] at the time points indicated on the graph (Figure 2D). First, the total number of pixels in the ROI, then a threshold of 35% was applied, and the pixel count after thresholding was noted. The condensation parameter (Y axis on Figure 2D) is defined as the percentage pixel count of the pixel number below 35% threshold divided by the total number of pixels in the ROI. Pixels below the applied threshold are proportional to chromosome condensation. The quantification pipeline was automated using a custom-built macro on Fiji to scale and threshold the image and calculate pixel count using the histogram function. Finally, the log values were normalized to 100% and arranged according to time series using MATLAB_R2020b.